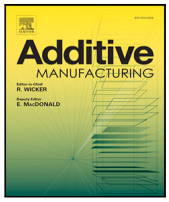
Additive Manufacturing 62 (2023) 103389



Contents lists available at ScienceDirect

Additive Manufacturing

journal homepage: www.elsevier.com/locate/addma



Research paper



Multi-length-scale study on the heat treatment response to supersaturated nickel-based superalloys: Precipitation reactions and incipient recrystallisation

Yuanbo T. Tang [a,*], Chinnapat Panwisawas [a,f], Benjamin M. Jenkins [a,1], Junliang Liu [a], Zhao Shen [a,2], Enrico Salvati [b,3], Yilun Gong [a,4], Joseph N. Ghoussoub [a], Stefan Michalik [d], Bryan Roebuck [e], Paul A.J. Bagot [a], Sergio Lozano-Perez [a], Chris R.M. Grovenor [a], Michael P. Moody [a], Alexander M. Korsunsky [b], David M. Collins [c], Roger C. Reed [a,b]

[a] Department of Materials, University of Oxford, Parks Road, Oxford, OX1 3PH, United Kingdom
[b] Department of Engineering Science, University of Oxford, Parks Road, Oxford, OX1 3PJ, United Kingdom
[c] School of Metallurgy & Materials, University of Birmingham, Birmingham, B15 2TT, United Kingdom
[d] Diamond Light Source Ltd., Harwell Science and Innovation Campus, Didcot, Oxfordshire, OX11 0DE, United Kingdom
[e] National Physical Laboratory, Hampton Road, Teddington, Middlesex, TW11 0LW, United Kingdom
[f] School of Engineering and Materials Science, Queen Mary University of London, London E1 4NS, United Kingdom

ARTICLE INFO

Keywords:
Precipitation kinetics
Recrystallisation
Additive manufacturing
Synchrotron
Superalloys
Atom probe tomography
Non-equilibrium

ABSTRACT

A supersaturated γ phase microstructure is produced in Ni-based superalloys using laser powder bed fusion (L-PBF) – the cooling rate arising from the process is shown to suppress the solid-state precipitation of the γ' phase. The response of the material to a heat treatment therefore requires new understanding at the fundamental level, since the first population of γ' precipitate forms upon heating, in contrast to cooling from homogenisation above the γ' solvus. Here, we have interrogated two new nickel-based superalloys designed for the L-PBF technology, both *in situ* and *ex situ*, at multiple length scales using advanced characterisation methods. First, we conducted *in situ* synchrotron X-ray diffraction during various heat treatments to trace the evolution of the γ' volume fraction with temperature. The first structural changes were detected at an unexpectedly low temperature of ~445 °C. Second, the temperature for γ' nucleation and its sensitivity to heating rate was studied using an electrical resistivity method. Then, the γ' composition upon heating, isothermal holding and cooling is analysed using atom probe tomography (APT), the result is rationalised by further scanning-transmission electron microscopy and nanoscale secondary ion mass spectroscopy. Finally, static recrystallisation during isothermal exposure was investigated, which occurs within minutes. This work sheds light on a new strategy of tailoring microstructure for additively manufactured superalloys by manipulation of the γ' precipitate distribution upon heating.

1. Introduction

For the nickel-based superalloys, existing processing practice involves the use of either investment casting, powder metallurgy or else an extensive series of thermal–mechanical working operations on vacuum induction melted material [1,2]. A subsequent heat treatment is then needed to optimise properties; however, this is particularly cumbersome. For example, careful and lengthy solutioning heat treatments close to the incipient melting temperature are needed to remove the extensive microsegregation inherited from the investment casting operation, so that the strengthening γ' precipitates are distributed uniformly [3]. For powder metallurgy or a cast & wrought component, a heat treatment at temperatures close to the γ' solvus is necessary to promote the consolidation of parts and patterns of recrystallisation, thus achieving desirable microstructures [4].

* Corresponding author.
E-mail address: yuanbo.tang@materials.ox.ac.uk (Y.T. Tang).
[1] Current affiliation: Univ Rouen Normandie, INSA Rouen Normandie, CNRS, Groupe de Physique des Matériaux UMR 6634, F-76000 Rouen, France.
[2] Current affiliation: School of Materials Science and Engineering, Shanghai Jiao Tong University, Shanghai 200240, China.
[3] Current affiliation: Polytechnic Department of Engineering and Architecture (DPIA), University of Udine, Via delle Scienze 208, Udine, 33100, Italy.
[4] Current affiliation: Max–Planck-Institut für Eisenforschung GmbH, Max–Planck Straβe 1, 40237, Düsseldorf, Germany.

https://doi.org/10.1016/j.addma.2023.103389
Received 7 October 2022; Received in revised form 6 December 2022; Accepted 2 January 2023
Available online 7 January 2023
2214-8604/© 2023 The Authors. Published by Elsevier B.V. This is an open access article under the CC BY license (http://creativecommons.org/licenses/by/4.0/).

Table 1
As-fabricated alloy compositions for current study in wt-% & at-% (Ni-base), measured using ICP-OES, ICP-combustion (carbon).

	Ni	Cr	Co	Al	Ti	Nb	Ta	W	Mo	C	B
ABD-900AM (wt%)	Bal	16.03	18.77	2.17	2.47	1.81	1.15	3.26	2.15	0.044	0.005
ABD-850AM (wt%)	Bal	18.68	17.87	1.41	2.64	0.48	0.28	5.24	2.06	0.042	0.005
ABD-900AM (at%)	Bal	17.95	18.55	4.68	3.00	1.13	0.37	1.03	1.30	0.21	0.03
ABD-850AM (at%)	Bal	21.08	17.79	3.07	3.24	0.30	0.09	1.67	1.26	0.21	0.03

When additive manufacturing (AM), commonly known as 3D-printing, is employed, the situation is radically different [5–8]. Both starting powder stock from atomisation and subsequent layer-by-layer fusion processes involving a high power density and a low residence time of the heat source [9,10] that yields heat transfer characteristics conferring very fast cooling rates (1-40 $\times$ 10^6 K/s) [11]. Provided that the alloy composition is chosen appropriately and despite the repeated thermal cycles, the γ' precipitation reaction can then be suppressed in the powder form and/or in the printed material which comprises γ alone rather than a γ/γ' mixture as seen conventionally [12–14]. Segregation behaviour also occurs along cell boundaries at a smaller length-scale, i.e. micron or sub-micron scale [15–18], in contrast to over 100 μm observed from casting [19]. As a result, the diffusion-assisted homogenisation process is presented with a much reduced diffusion path of two to three orders of magnitude. Hence, it leads to an interesting quest: can the high temperature homogenisation treatment near melting be shortened or even avoided? Indeed, many reports have indicated that AM processed heritage alloys may not necessarily yield optimal properties with the traditional heat treatment parameters, even with flawless processing [20,21]. Clearly, the significant change in the initial microstructure inherited from the AM process presents an opportunity – and a necessity – to think completely differently about the way microstructure is used to confer properties.

The research reported in this paper was motivated with the above in mind. There is a need for fundamental studies associated with the γ' precipitation kinetics from a super-saturated solution since the first population of γ' precipitates generated from the L-PBF route is via heating, rather than from cooling. Secondary effects from heat treatment such as recrystallisation for anisotropy removal are of significance as well [22]. Here, we have interrogated the subtle variation in response to temperature, both structurally and chemically, by a combination of characterisation techniques. First, scanning transmission electron microscopy (STEM) and atom probe tomography (APT) were used to determine the initial microstructure. The γ' precipitation kinetics were then determined using time-resolved synchrotron diffractometry alongside unique electrical resistance measurements. High resolution microscopy was utilised to reveal phase transitions, recrystallisation behaviour and to determine chemical evolution in detail. Finally, we discuss the implications to heat treatment and possible new strategies.

2. Experimental methodologies

2.1. Materials and fabrication

Two new superalloys designed specifically for additive manufacturing, ABD-900AM and ABD-850AM, were selected for this study due to their promising component level applications [23]. The materials were first argon gas atomised by the Aubert & Duval company by making use of a pre-alloyed ingot produced by vacuum induction melting; this yielded a median powder size of 34 μm, where D10 and D90 are 21 and 56 μm respectively. A Renishaw AM 400 machine was employed to produce vertical rectangular bars with dimensions of 10 $\times$ 10 $\times$ 52 mm^3. The laser was operated in a modulated (pulsed) mode at 200 W with a speed of 0.8 m/s and a spot size of 70 μm, with the recoating layer thickness of powder set at 30 μm. The scanning strategy was a raster scan with 67° rotation between each successive layer. More details on the processing procedure can be found in [24]. The final bulk materials were fully dense.

The chemical composition after additive manufacture was measured using inductively coupled plasma (ICP) based methods including optical emission spectroscopy (OES) and combustion analysis, see Table 1. The sulphur content determined by the combustion method for the bulk materials is below 0.003 wt%; the manufacturer reported the sulphur level is below 0.0015 wt% in powder form by LECO analysis. CALPHAD calculations (under equilibrium condition) with TCNI8 database suggest they contain ~0.35 and 0.25 of γ' in volume fraction for ABD-900AM and ABD-850AM, respectively [13].

2.2. Synchrotron X-ray diffraction (S-XRD) and analysis

Time-resolved synchrotron radiation experimentation was carried out on the I12 high energy X-ray beamline at the Diamond Light Source (UK) [25]. A Linkam TS1500 furnace was used for heat treatments and a Pilatus 2M CdTe 2D area detector was utilised to acquire diffraction data in a transmission geometry. The specimen was located ~1.6 m away from the detector and was positioned in a furnace, where a flow of argon gas was provided throughout the heat treatment to minimise oxidation. The experimental setup adapted here has been proven in a prior study [26]. The true temperature was calibrated from knowledge of the ABD-900AM behaviour, i.e. 1080 °C for the γ' solvus temperature [13]. The Linkam furnace temperature is approximately 50 °C higher than the true temperature at this point. The difference between the two temperatures is assumed to follow a linear relationship. The diffraction patterns were collected using an X-ray energy of 80.291 keV calibrated with a CeO_2 standard [27], with a beam size fixed at 500 μm $\times$ 500 μm, at a data acquisition rate of 2 Hz. For the initial as-fabricated microstructure, a long exposure of 600 s was performed for each material to reveal any minor phases. 2D diffraction images were azimuthally integrated into intensity curves as a function of a scattering vector, Q, employing the DAWN software [28,29]. During this procedure, a mask file was first applied to each raw image to remove data associated with dead pixels or detector module gaps. The integrated datasets were subsequently analysed using in-house code based upon MATLAB software. Individual reflections were firstly isolated and any background intensity was subtracted using a second order polynomial (fitting to data points far away from the tails of the reflections). Both superlattice and fundamental reflections were fitted with Pseudo-Voigt functions, with the former comprising the $\{100\}_{\gamma'}$ reflection which was used to infer the line profile position and shape of the $\{200\}_{\gamma'}$. As the lattice parameters of the γ and γ' phases are near identical, their measurement is possible by constraining the $\{200\}_{\gamma'}$ line profile, and fitting the remaining fundamental reflection intensity to obtain the $\{200\}_{\gamma}$ d-spacing, following Stone et al. [30]. It is noted that there were no weak reflections from minor phases in the tails of the $\{100\}_{\gamma'}$ or $\{200\}_{\gamma/\gamma'}$ reflections that would affect the fitting procedure. Integrated peak intensities and d-spacings were extracted from the fitted line profiles and were used to identify the volume fraction of phases and the γ/γ' lattice misfit. The volume fraction was calculated from ratios of the integrated intensities of the $\{200\}_{\gamma}$ and $\{200\}'_{\gamma}$ peaks, with each peak corrected for the chemistry dependent structure factor. The temperature dependent compositions of the γ and γ' phases were estimated from CALPHAD simulations described previously. The method and suitability of this approximation is described elsewhere [26]. The breadth, β, of the reflections was also recorded; this arises from the broadening of the sample and the instrument. Error bars are calculated based on the difference between the broadening

Table 2
Heat treatment parameters used for the time-resolved synchrotron experiment for ABD-850AM and ABD-900AM in sub-solvus and super-solvus conditions for various heating and cooling rates.

		Heat	Dwell	Cool
ABD-900AM	sub-solvus	RT → 1050 °C at 1 K/s	1050 °C/60 min	1050 °C → RT at 1 K/s
	super-solvus 1	RT → 1165 °C at 1 K/s	1165 °C/60 min	1165 °C → RT at 1 K/s
	super-solvus 2	RT → 1220 °C at 0.1 K/s	1220 °C/60 min	1220 °C → RT at 0.1 K/s
ABD-850AM	sub-solvus	RT → 1000 °C at 1 K/s	1000 °C/60 min	1000 °C → RT at 1 K/s
	super-solvus 1	RT → 1165 °C at 1 K/s	1165 °C/60 min	1165 °C → RT at 1 K/s
	super-solvus 2	RT → 1165 °C at 0.1 K/s	1165 °C/60 min	1165 °C → RT at 0.1 K/s

at a given time, relative to the final breath. This approach provides a qualitative approximation to the lattice parameter variation.

All samples were first prepared by electrical discharge machining (EDM) into discs of 3 mm diameter and 0.5 mm thickness, which were then ground by abrasive media to remove any recast layer. In order to take account for the {001} texture in the as-fabricated material, all tests were carried out with the X-ray beam parallel to the build direction. No preferred orientation was observed for the samples in this orientation, giving diffraction rings with a uniform intensity distribution as a function of azimuthal angle. Both materials were subjected to three types of heat treatment to investigate the phase transformation and corresponding structural changes during heating, isothermal holding and cooling. The heating & cooling rates were chosen to be 1 K/s and 0.1 K/s, to understand the rate dependency on the phase transformations within the industrial relevant heat treatment range. Isothermal hold temperatures were selected to be either below (sub-solvus) or above (super-solvus) the γ' solvus, to provide *in situ* evidence of structural evolution during the isothermal hold. Details of the heat treatment parameters used for the study are summarised in Table 2.

2.3. Electrical resistivity measurements

Electrical resistivity measurements were made during the heat treatments using an electro-thermal mechanical testing (ETMT) system. Tensile samples of 40 mm length were mounted between two water-cooled grips. A Type-K thermocouple was spot welded at the centre to control temperature, and two negative wires (Ni-2Al-2Mn-1Si) of Type-K thermocouple were spot welded 1.5 mm each side from the thermocouple as potential contacts where the temperature distribution is uniform [31]. During heating and cooling, a zero load was maintained on each sample to prevent a resistance change induced by deformation [32]. Hence the change of resistivity can be solely interpreted by the phase transition that occurred during heat treatment [33], i.e. the γ/γ' reaction in this case where the precipitate phase obtains a higher resistivity value [34]. The heating and cooling cycle was given to ABD-900AM for the super-solvus 1 heat treatment is consistent with the synchrotron experiment listed in Table 2. In addition, to compare the difference in the as-fabricated material vs heat treated material, the same heat treatment was applied to the specimen twice. The second heat treatment cycle is assumed to start with γ' precipitates present in the microstructure from the end of the first cycle. Moreover, the effect of the heating rate on the transformation was also investigated with four heating rates at 0.1, 1, 10 and 100 K/s.

2.4. Microscopy and characterisation

2.4.1. Scanning electron microscopy

A Zeiss Merlin field emission gun scanning electron microscope (FEG-SEM) was used to characterise the microstructural evolution in the specimens, particularly the cellular structure and γ' precipitates. After conventional metallographical preparation, the specimens were electrolytically etched with 10% phosphoric acid at room temperature with 3 V DC. A secondary electron detector was used to assess the evolution of γ' precipitates post heat treatment. The SEM was operated at 15 kV with a probe current of 5 nA and the plane of characterisation was perpendicular to the build direction. Their sizes were measured using ImageJ software after binarisation. For comparison, the as-fabricated material and the fully annealed material (1220 °C/4h/AC) were also characterised as references. The grain orientations and texture were also quantified using the electron backscattered diffraction (EBSD) technique. A Bruker e-Flash^{HR} detector was utilised, where for low resolution scanning, the diffraction patterns were stored in 160 × 120 pixel^2 resolution at a step size of 2.23 μm. Recrystallisation fraction and texture component was analysed using HKL Channel 5 software package.. For ABD-850AM (super-solvus 2, recap Table 2), a high-resolution map was scanned in 800 × 600 pixel^2 resolution at a step size of 0.45 μm in 16 bits. The patterns were then analysed using a cross-correlation based technique [35,36] for the distribution of geometrically necessary dislocation (GND) density [37].

2.4.2. Scanning transmission electron microscopy energy dispersive X-ray spectroscopy

Elemental segregation in the as-fabricated microstructure was determined using scanning transmission electron microscopy energy dispersive X-ray spectroscopy (STEM-EDS) and high-angle annular dark-field (HAADF) detector. Metallic foils were prepared using a twin-jet electropolishing unit to less than 100 nm. Electropolishing was conducted using an electrolyte of 5% perchloric acid ($HClO_4$) in methanol at −40 °C. Chemical composition analysis were conducted on a JEOL ARM200F (cold-field emission gun) operating at 200 kV and equipped with an Oxford Instrument EDX100 detector. The step sizes for EDX mapping and line-scanning were set to be 24 and 3 nm, respectively.

2.4.3. Atom probe tomography (APT)

Samples were mechanically ground and polished before being prepared for atom probe tomography (APT) analysis using standard focused-ion beam (FIB) lift-out methods [38,39]. A dual-beam Zeiss Crossbeam SEM/FIB was used to deposit a protective layer of Pt onto the sample (initially using electron beam deposition and then using ion beam deposition). Trenches were milled using Ga ions, with an accelerating voltage of 30 kV and initial current of 7 nA, whilst undercuts were performed using a beam current of 700 pA. Preliminary tip shaping was conducted at 700 pA and final sharpening at 50 pA was used to achieve a tip with a radius of under 100 nm. In order to minimise Ga implantation into the final APT volume, a polishing stage was conducted at 2 kV to remove approximately 300 nm from the apex of each tip [39]. Atom probe analyses were conducted on a LEAP 5000 XR. Analyses were conducted at 50 K and in laser-pulsing mode, using a 355 nm wavelength UV laser and a pulse energy of 40 pJ. Pulse repetition rates were automatically adjusted throughout the course of the experiment such that ions with a mass-to-charge-state ratio of up to 120 Da were collected. Reconstructions were performed using Cameca's IVAS software 3.8.8.

2.4.4. Nanoscale secondary ion mass spectrometry (Nano-SIMS)

SIMS measurements were conducted with a Cameca Nano-SIMS 50 ion probe instrument. The double-focusing secondary ion mass spectrometer employed here is capable of a high lateral resolution to ~50 nm for the Cs+ primary ion source. Primary ions were accelerated

Table 3
Compositions of ABD-900AM in the as-fabricated state in at-% (Ni-base), measured using APT. Note no S was detected in the dataset.

	Ni	Cr	Co	Al	Ti	Nb	Ta	W	Mo	C	B	Phase
Tip 1	Bal	19.38	20.19	4.81	2.66	0.89	0.41	0.93	1.20	0.00	0.01	γ
Tip 2	Bal	19.76	20.35	4.49	2.82	0.89	0.38	0.81	1.07	0.02	0.01	γ
Tip 3	Bal	19.02	20.40	4.44	2.41	0.80	0.38	0.92	1.13	0.01	0.00	γ
Tip 4	Bal	19.75	19.95	4.64	3.01	1.07	0.44	0.96	1.27	0.02	0.01	γ

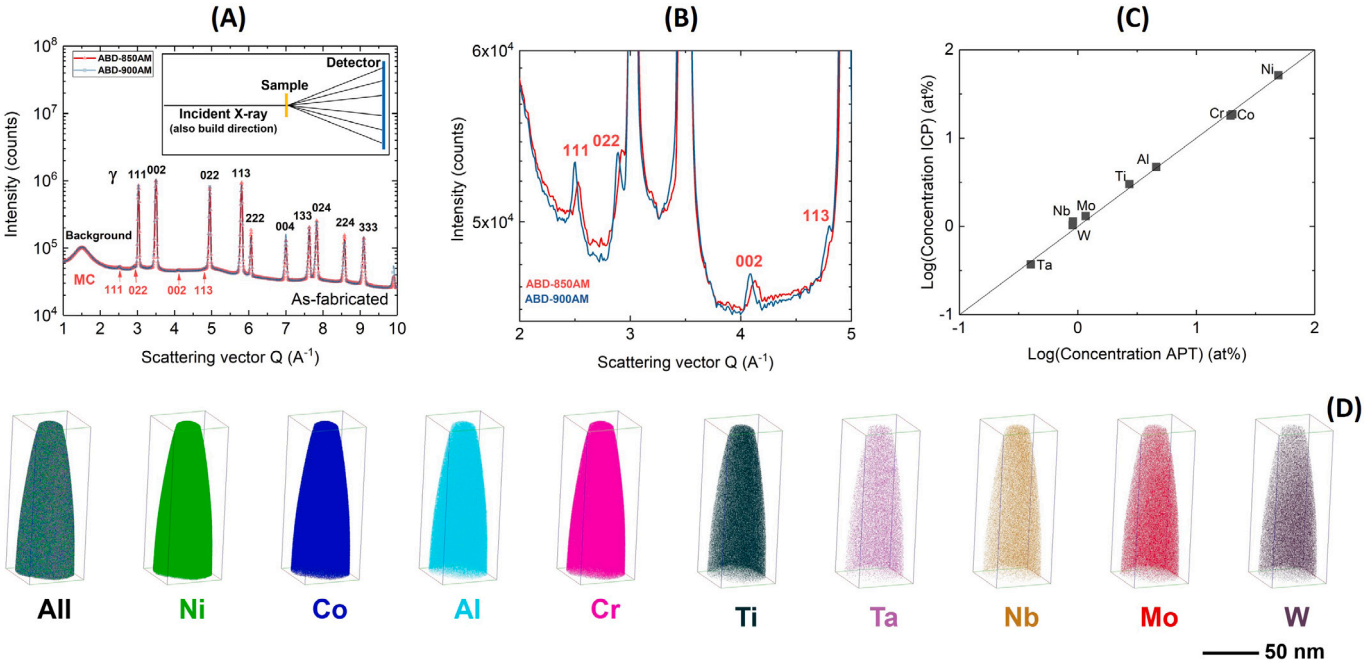


Fig. 1. Structural and compositional characterisation of the as-fabricated ABD-850AM and ABD-900AM. Synchrotron X-ray diffraction of ABD-850AM & ABD-900AM (a) with 600 s exposure and a zoom-in of the MC carbide reflections (b). Regression of elemental concentration measured using both ICP-OES method and APT analyses averaged over four tips (c). Reconstructed elemental maps measured with APT of the as-fabricated ABD-900AM showing no phase separation (d).

at +8 kV, where the sample was held at −8 kV that yields a primary beam energy of 16 keV. Three samples were characterised in this condition, including as-fabricated, sub-solvus and supersolvus heat treated sample (no ageing). For each map, signals of four secondary ions were detected simultaneously, those are ^{12}C, $^{11}B^{16}O_2$, ^{32}S and ^{18}O, for chemical distribution of carbon, boron, sulphur and oxygen respectively. The scan raster size was chosen at 12 × 12 μm^2 or 30 × 30 μm^2 and dwell time per pixel of 2 ms, the step sizes for each map was 47 and 117 nm. The procedure of the SIMS measurements and analysis was detailed elsewhere [40].

2.5. Vickers micro-hardness measurement

The hardness in the as-fabricated state has been compared to that after long-term exposure (500 °C for 120 h). A Wolpert micro-hardness machine was employed. The measurement was carried out with a Vickers indenter at a load of 0.3 kgf applied to the sample for 10 s Five tests were completed at each condition to ensure statistical significance.

3. Results

3.1. Super-saturated γ-matrix & cellular segregation

The initial microstructure produced by the L-PBF process is first characterised. Fig. 1(a) reveals the phases present in the long exposure S-XRD measurements for both ABD-850AM and ABD-900AM in the as-fabricated state. Both materials possess almost identical peak intensities for the majority of the γ reflections; however, ABD-900AM shows slightly higher intensities for the MC carbide reflection (b). No γ' phase was detected within the sensitivity permitted by the technique. Further transmission-based electron microscopy results also did not observe the presence of γ', see Supplementary Figure S1. The chemical composition of ABD-900AM was also analysed using APT at four random dendrite cores to check whether phase separation could be detected. The reconstructed results highlighting the spatial distribution of all and each individual element are illustrated in Fig. 1(d). No carbon or boron was detected in these tips, as will be shown by Nano-SIMS maps in the following, suggesting the probed area does not contain any cellular or grain boundaries where the metalloids are preferentially located. In addition, the frequency distribution analysis fits well with the random (binomial) distribution suggesting no obvious clustering or long range order — phase separation was not detected within those APT tips, see Supplementary Figure S2.

As the APT lift-out locations were selected at random with no correlated transmission electron microscopy and due to the relatively small microstructural volumes sampled in each APT analysis, there exists a slight possibility that the sampled volume was composed of pure γ phase adjacent to a γ' precipitate. In order to eliminate this possibility, the concentration of each element was compared between ICP-OES (Table 1) and APT (Table 3) analysis in a $\log_{10}$-$\log_{10}$ plot, see Fig. 1 (c). A strong correlation is established between the two measurements. It confirms the APT tips have analysed the super-saturated γ phase, instead of the γ phase in a γ/γ' matrix. The latter case would otherwise skew the correlation very significantly, where an example is shown in the supplementary Figure S3 on the same material. Consequently, it is jointly suggested by S-XRD and APT that the as-fabricated superalloys are composed of only super-saturated γ phase with no detectable γ'. A critical cooling rate necessary for full γ' suppression is believed to

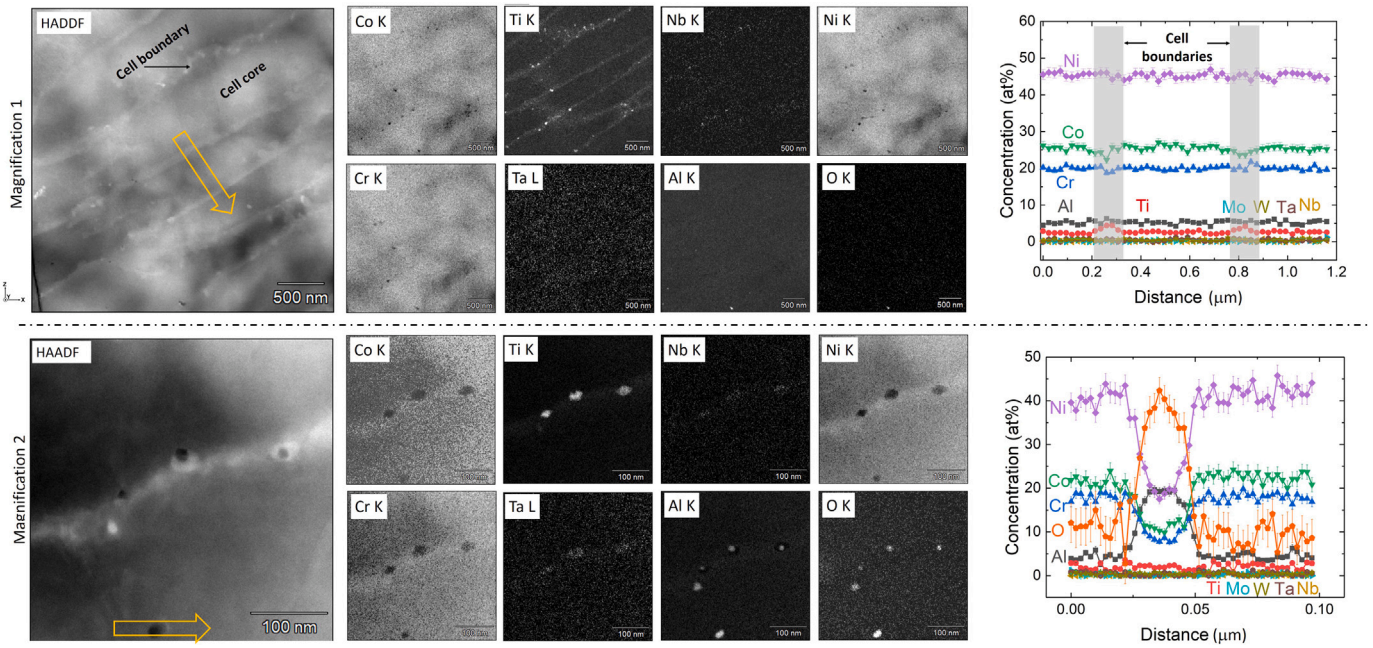


Fig. 2. Elemental net count maps obtained by scanning transmission electron microscopy energy dispersive X-ray spectroscopy (STEM-EDS) at two magnifications on as-fabricated ABD-900AM and associated quantitative line scans (orange arrows). (For interpretation of the references to colour in this figure legend, the reader is referred to the web version of this article.)

lie between that for electron beam melting (10^3–10^4 K/s) [6,41] and selective laser melting (10^6 K/s) [11], where the former method can induce fine γ' in the as-fabricated state [6].

Despite the γ/γ' transformation being suppressed, there was a discrepancy between the ICP-OES and APT analysis. This implies that local segregation may have emerged on a length-scale slightly larger than is visible via APT. Elemental mapping using STEM-EDS showing net counts (with background subtraction) in Fig. 2 revealed a site preference for each element with quantitative line scans (orange arrow). From the EDS mapping shown in Fig. 2, there is a clear Ti segregation to the cell boundaries, with Nb and Ta showing a much weaker trend, barely above noise levels. Other elements do not show a significant trend. A closer investigation at a cell boundary reveals some Ti, Nb, Ta and Al rich particles. HAADF imaging suggests two phases are present due to atomic contrast — Ti, Nb and Ta rich precipitates and Al rich precipitates. In order to complement the uncertainty of light element detection, especially carbon and boron, Nano-SIMS measurements were conducted. Fig. 3(a) shows the carbon, boron, oxygen and sulphur distribution in the as-fabricated state. Clearly, many carbon particles are observed; the distribution also demonstrates a directionality that is parallel to the cellular alignment in its corresponding SE image. Considering the transition metal enrichment at cell boundaries, those carbon particles are believed to be carbides, and are mostly likely to be the Ti/Nb/Ta rich MC type, as reported on similar alloys [42,43]. In addition, the boron map is similar to carbon whose distribution exhibits the same directionality, however, its presence is found both in particles and segregation to cell boundaries, consistent with reports elsewhere [44]. It is likely that some boride are present, though no correlative diffraction information can help pinpoint the compound type. Sulphur on the other hand is observed in particles as well. Although it is much lower in the net count in comparison, some form of sulphide is likely to exist in the microstructure within this small batch material. The oxygen map, on the contrary, shows no clear distributions. This does not rule out the possibility of very small oxides being present as the spot size was 47 nm for SIMS, hence any oxide below 100 nm cannot be reliably resolved. Indeed, the STEM EDS in Fig. 2 revealed that Al and O rich particles are much smaller than the carbide, strongly suggesting the presence of Al oxide particles after laser fabrication.

3.2. Precipitation kinetics by time-solved S-XRD

The evolution of the γ' phase with respect to the volume fraction and its first order derivative are presented in Fig. 4 as a function of time (a-c) and temperature (d-f). The heat treatment adopted here was consistently 1 K/s for heating and cooling with an isothermal hold for 60 mins, see Table 2. The heat treatment profiles are also plotted on the secondary (right) y-axis that overlays in Fig. 4(a-c). For sub-solvus ABD-900AM shown in Fig. 4(a), it is clear that there is no significant change in the volume fraction of γ' until a rapid increase is seen at ~740 °C, whereas the volume fraction peaked at ~915 °C, which then dropped to a constant value during the isothermal holding period of 60 mins. The cooling from isothermal holding is followed by a sudden increase in volume fraction. The rate of the reaction is illustrated using its first order derivative, dV_f/dt. The transformation rates increase initially with heating and peaks at ~809 °C. It changes sign from increasing to decreasing, and $dV_f/dt = 0$ at ~920 °C. From cooling, the reaction rate reached a local maximum at ~972 °C until the kinetics become more sluggish as it cools further. Although some evolution of γ' volume fraction is evident below 700 °C, this is probably a very small amount. The onset of the first population of γ' will be discussed in Section 4.1.

For sub-solvus heat treated ABD-850AM in Fig. 4(b & e), the evolution of the precipitation reaction follows a very similar trend to ABD-900AM. The rapid increase of volume fraction is found at 824 °C. The volume fraction reaches a peak at 938 °C which maintained constant during the isothermal period. The transformation rate is fastest at ~852 °C during heating and at ~940 °C upon cooling.

Super-solvus 1 heat treatment was also conducted to fully dissolve the precipitates above the γ' solvus temperature, and to reform γ' upon cooling that is employed conventionally. Fig. 4(c) shows the precipitate evolution of ABD-900AM up to 1165 °C. The volume fraction was first held constant with heating until a significant increase emerged at ~724 °C; it reaches a local maximum at ~917 °C and is followed by a decrease to zero at isothermal holding. Fig. 4(f) illustrates the evolution as a function of temperature that helps to interpret the kinetics (dV_f/dT) more clearly. The fastest transformation rate occurred at ~788 °C during heating and ~1026 °C upon cooling.

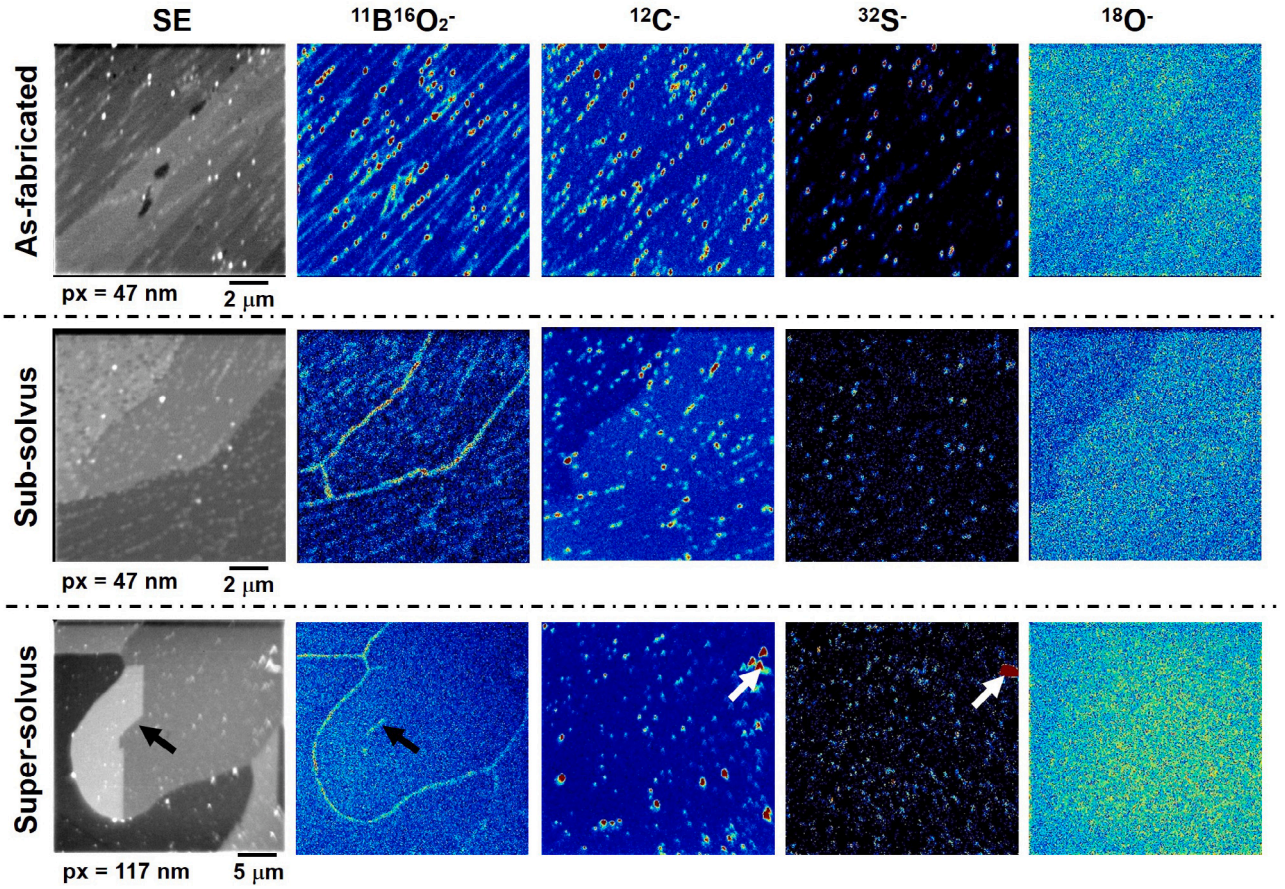


Fig. 3. Elemental maps of C, B, O and S obtained by secondary ion mass-spectroscopy (Nano-SIMS) on as-fabricated, sub-solvus & super-solvus ABD-900AM.

An isothermal hold at 1165 °C did not successfully trigger recrystallisation as expected [13]. This motivated a further supersolvus heat treatment at a higher isothermal hold of 1220 °C. Notable changes to the diffraction pattern were identified; large spots were observed after a few minutes. This is attributed to fewer larger grains diffracting more strongly in certain orientations. It suggests grain growth within the microstructure which must have followed the static recrystallisation. Nevertheless, the original assumption for powder diffraction with many crystals diffracting is violated to some extent, and the azimuthal integration no longer can reliably interpret the subtle variation in the superlattice reflection for the spotty pattern (due to far fewer grains present). For this reason, the evolution of precipitation was not studied further when recrystallisation took place as it cannot be accurately determined. Instead, the recrystallisation behaviour is studied in more depth.

3.3. Evolution of lattice misfit

The lattice parameter and its associated misfit development has been studied for both alloys during the sub-solvus heat treatment. Fig. 5(a-b) demonstrates the lattice parameter of γ (black curve) and γ' (red curve) with time. The γ' lattice parameter is analysed starting from 800 °C when the superlattice peak is first clearly distinguishable. The corresponding error bars are also given, as described in Section 2.2. For superalloy microstructure, the γ/γ' interface is coherent with a cubic-to-cubic orientation relationship [1], i.e. $\{100\}_{\gamma}//\{100\}_{\gamma'}$. Therefore, the lattice misfit (δ) is defined as below, where a_{γ} and $a_{\gamma'}$ are the lattice parameters of each phase:

$$\delta = \frac{2(a_{\gamma'} - a_{\gamma})}{(a_{\gamma'} + a_{\gamma})}$$

For the γ' precipitates, the lattice constant started from 3.72 Å at 800 °C, which contributed to an exceptionally large lattice misfit of over 25×10^{-3} and with a great scatter initially, see Fig. 5(c-d). This is about an order of magnitude higher than most superalloys from conventional routes, such as CMSX-4 [45], AM1 [46], Astra1 [47], which is in the range of $\pm$ 4 $\times$ 10^{-3}. Following further heating, a drastic decrease of lattice misfit is observed for both materials. The mismatch also decreases slightly during isothermal holding, and then increases moderately during the final cooling to room temperature. It is worth noting that the misfit for the final microstructure at ambient temperature ($< 2.5\times 10^{-3}$) never reaches the same level compared to the initial state of heating ($>25 \times 10^{-3}$).

3.4. Post-mortem microstructure evolution: γ' morphology, recrystallisation and trace element segregation

The microstructure after light etching at each processing stage is presented in Fig. 6: as-fabricated, sub-solvus, super-sovlus 1 & 2 and fully annealed respectively. For both ABD-900AM and ABD-850AM, a very similar trend of γ' size and morphology is observed. In the as-fabricated state, no γ' precipitation was found in either alloy — instead a cellular structure with carbides and borides decorating the cell boundaries. For the sub-solvus heat treatment, spherical γ' precipitates developed and its distribution shows distinctive cell patterns, i.e. a preferential site at the inter-cellular regions. Furthermore, a few precipitates can be observed in the centre of some of the cells developed (Fig. 6). In addition, precipitation size is coarser in ABD-900AM (110 nm) compared to ABD-850AM (67 nm), which is a trend consistent with all other cooling conditions. For the super-solvus conditions, such circular patterns indicating previous cell locations are no longer observed consistent with homogenisation having taken place. The cooling

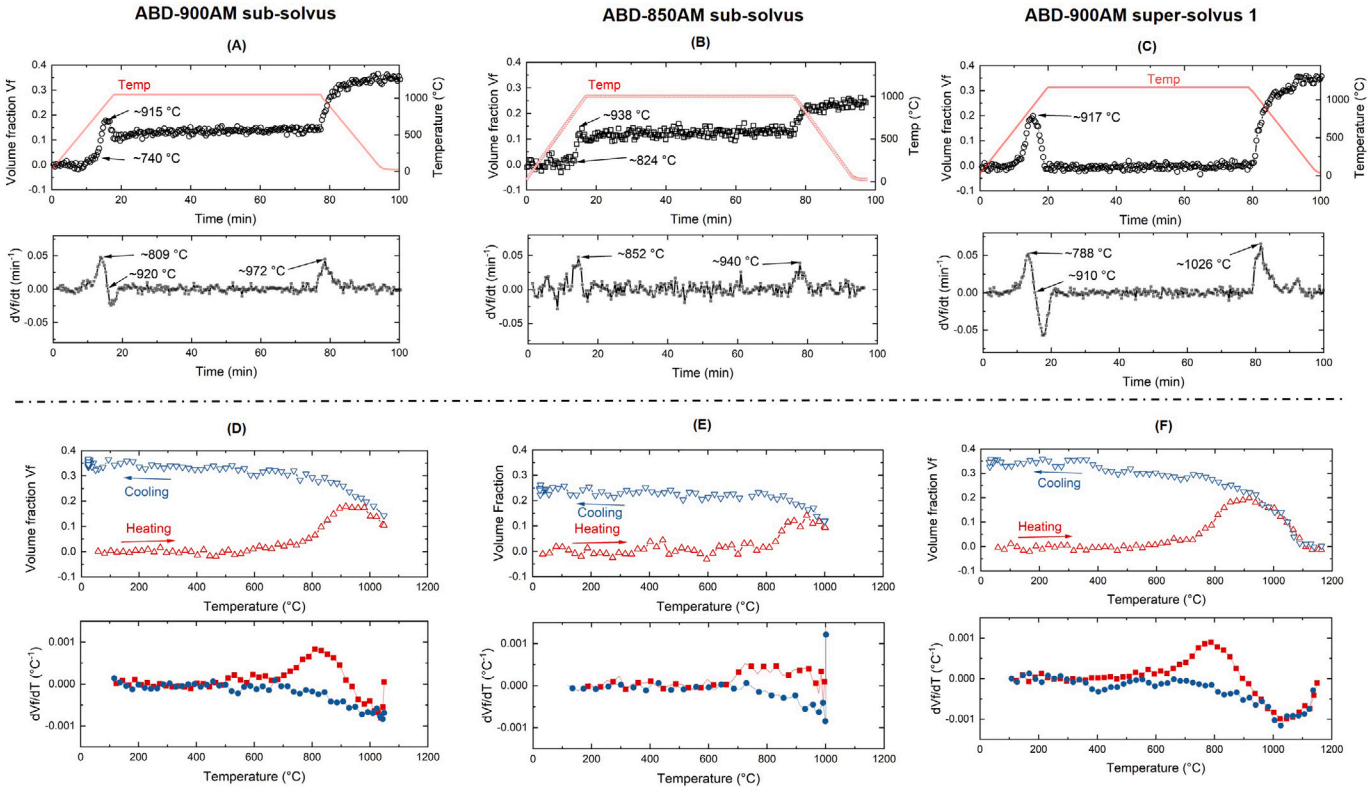


Fig. 4. Evolution of γ' precipitate volume fraction under sub- & super-solvus 1 heat treatment for ABD-900AM and ABD-850AM. Evolution of volume fraction and its first order derivative as a function of time (a-c) and temperature (d-f). All heating and cooling rates were consistent at 1 K/s. The equilibrium volume fractions are 0.35 and 0.25 respectively.

rate of 1 K/s led to the development of a higher number density and finer γ' precipitates, whereas 0.1 K/s cooling led to a sparsely distributed yet coarser precipitates, which is more apparent for ABD-900AM. In addition, the morphology has also changed from spherical to octo-dendritic with a lower cooling rate, consistent with reports elsewhere [1,48,49]. For the fully annealed sample (air cooling above solvus), precipitates obtain the smallest sizes amongst all conditions.

The grain structure and texture change was determined with the aid of EBSD at each condition, see Fig. 7. Inverse pole figure maps along the building direction (z-axis) and its corresponding pole figure demonstrate a strong texture of {001} poles, similar to the as-fabricated and sub-solvus state. As the heat treatment temperature increases, a clear texture breakdown emerges as a result of increasing recrystallisation fraction. Notably, the super-solvus 1 (at 1 K/s) was isothermally held at 1165 °C for both alloys, whereas partial recrystallisation occurred in ABD-850AM but not in ABD-900AM. On the contrary, a long hold at a higher temperature (fully annealed) completes the recrystallisation with drastic grain growth. Quantitative indices of both characteristics, i.e. {100} texture strength and recrystallisation fraction are demonstrated in Fig. 7(f) with respect to each heat treatment.

Segregation behaviour of the trace elements also shows significant changes during heat treatments, see Fig. 3. After sub-solvus heat treatment, the boron-rich particles disappeared suggesting boride dissolution, at least to a large extent. Boron segregation is still visible at the grain boundaries. Interestingly, the boron distribution also shows some distinctive patterns in each grain, which aligns with the γ' distribution in the SE image. Further APT result has confirmed this trend, see Supplementary Figure S4, where boron shows a much stronger tendency to reside in the γ' phase. Carbon, sulphur and oxygen maps do not show a large difference in comparison to the as-fabricated state in elemental distribution.

For the super-solvus case (air cooled), boron also demonstrates strong segregation tendency to grain boundaries. Interestingly, it shows the interface plane normal has some influence on local segregation. As denoted by the black arrows, some sections in the same grain boundary shows more local segregation than in other sections. No distinctive patterns were found for γ' precipitates this time, which is likely due to a combination of an increased spot size (117 nm) and smaller precipitation size (air cooling). In addition, both sulphur and carbon can be found together (see white arrows) in this condition, suggesting the possible formation of carbo-sulphide.

3.5. Effect of heating rate on γ/γ' reaction

The kinetics of the diffusion-assisted precipitation is sensitive to heating rate, so further electrical resistance measurements were conducted to develop an extended understanding of the heating rate effect from 0.1, 1, 10 & 100 K/s using an ETMT machine.

The identical heating and cooling cycle as the synchrotron experiment were conducted for ABD-900AM at 1 K/s, see super-solvus 1 in Table 2. To exemplify any differences between the as-fabricated microstructure in contrast to the heat treated microstructure, the same heating and cooling cycle was performed again. A resistivity inflection is induced by structural change by either a phase transition and/or deformation [33,50]. For superalloys, a zero-load resistivity measurement is frequently used to interpret the γ/γ' reaction [32] due to a difference in resistivity between the γ and γ' phases, where the latter obtains a higher value [34]. Fig. 8(a-b) shows the resistivity evolution of ABD-900AM during heating and cooling for two complete cycles. The first heating cycle shows a moderate upward slop up to just below 500 °C when a significant increase in the resistance is observed. As the temperature further increases, the resistance reaches a maximum at ~780 °C and then decreases rapidly until just over 1000 °C. The drastic increase in resistance ~500 °C denotes the nucleation of the γ' phase and the decrease at just over 1000 °C indicates the precipitation dissolution. For the second heating and cooling cycle shown in Fig. 8 (b), the resistance almost overlaps with each other suggests the microstructure has reached equilibrium. The only discrepancy is observed at ~1000 °C,

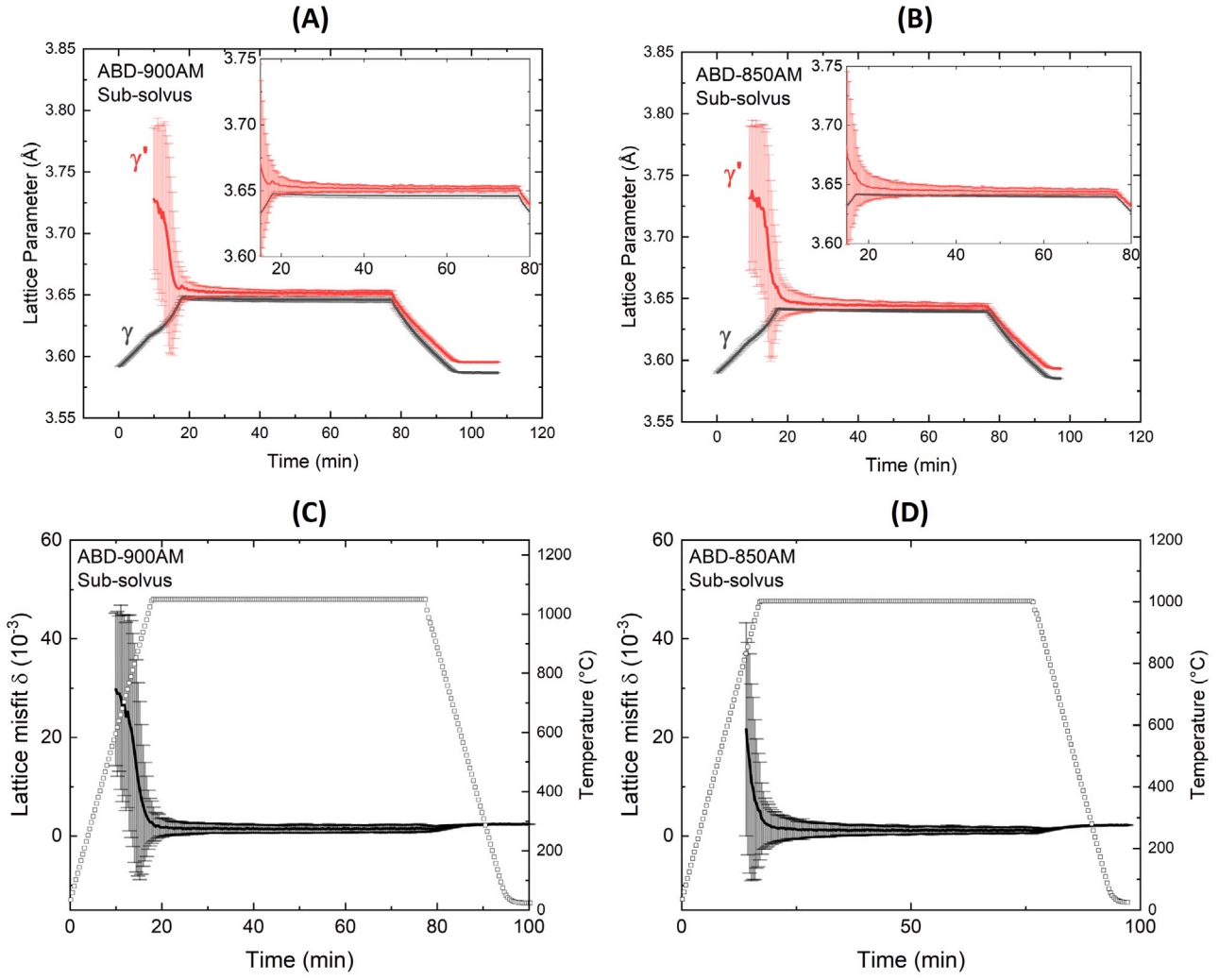


Fig. 5. Lattice parameter evolution of γ (black) and γ' (red) as a function of time for ABD-900AM and ABD-850AM (a & b). A lattice parameter decrease is observed during isothermal holding as shown in magnified inset plots. The lattice misfit between the two phases is illustrated as a function of temperature for both materials (c & d). (For interpretation of the references to colour in this figure legend, the reader is referred to the web version of this article.)

which is manifested by the undercooling between the γ' dissolution and its re-precipitation.

For the identification of the onset temperature of the resistance increase, the drastic increase of resistance from the first heating curve is analysed. Both the immediate onset and tangent constructions were used, as illustrated in Fig. 8(c). The influence of the γ' onset temperature is shown in Fig. 8(d). The onset temperature correlates strongly with the heating rate.

4. Discussion

So far, fundamental insights have been gleaned into the mechanism of γ' precipitate from a fully suppressed supersaturated γ matrix. Nevertheless, there are a few questions which needed further rationalisation to establish sound mechanistic understanding. For instance, at what temperature did the γ' start to incubate upon heating? What structural and compositional evolution are associated during γ/γ' reaction? Does isothermal holding induce measurable change of precipitation despite no variation in volume fraction — is it necessary? Why is the recrystallisation start temperature much higher than a traditional route? The following sections will focus on addressing those questions to amplify the findings with detailed analysis and further experiments where necessary.

4.1. Embryonic development of γ' upon heating

The critical temperature for the first γ/γ' reaction upon heating is worth further attention. The onset temperatures quoted in Section 3.2 of 740 °C for ABD-900AM and 824 °C for ABD-850AM was determined by a tangent construction of the V_f vs T plot [51]. It is certain that the γ' has formed at these points. However, this tangent construction can be an over-estimate as it ignores any initial partial transition which can be sluggish and time dependent; it is also associated with a higher uncertainty while examining the weak {001} superlattice reflection. Alternatively, the structural change by examining the {111} fundamental reflections of the γ matrix that yields much less uncertainty. As such, Fig. 9 shows the γ lattice parameter (a) change during heating for both alloys. A clear slope change is observed at approximately 500 °C. The first order derivative, $\frac{da}{dT}$ vs T, is used to identify the onset of the transition. A sharp change is observed at ~445 °C, which suggests the first structural change during heating.

The temperature for triggering this structural change was unexpectedly low. To understand better the nature of the kink in the lattice parameter, a long thermal exposure at 500 °C for 120 h was carried out followed by chemical and hardness measurement. One atom probe tip was extracted at the cell core from this specimen. Although no γ' precipitate was observed in this tip, a subtle change in solute content was observed, especially an increase of W, see Supplementary Figure

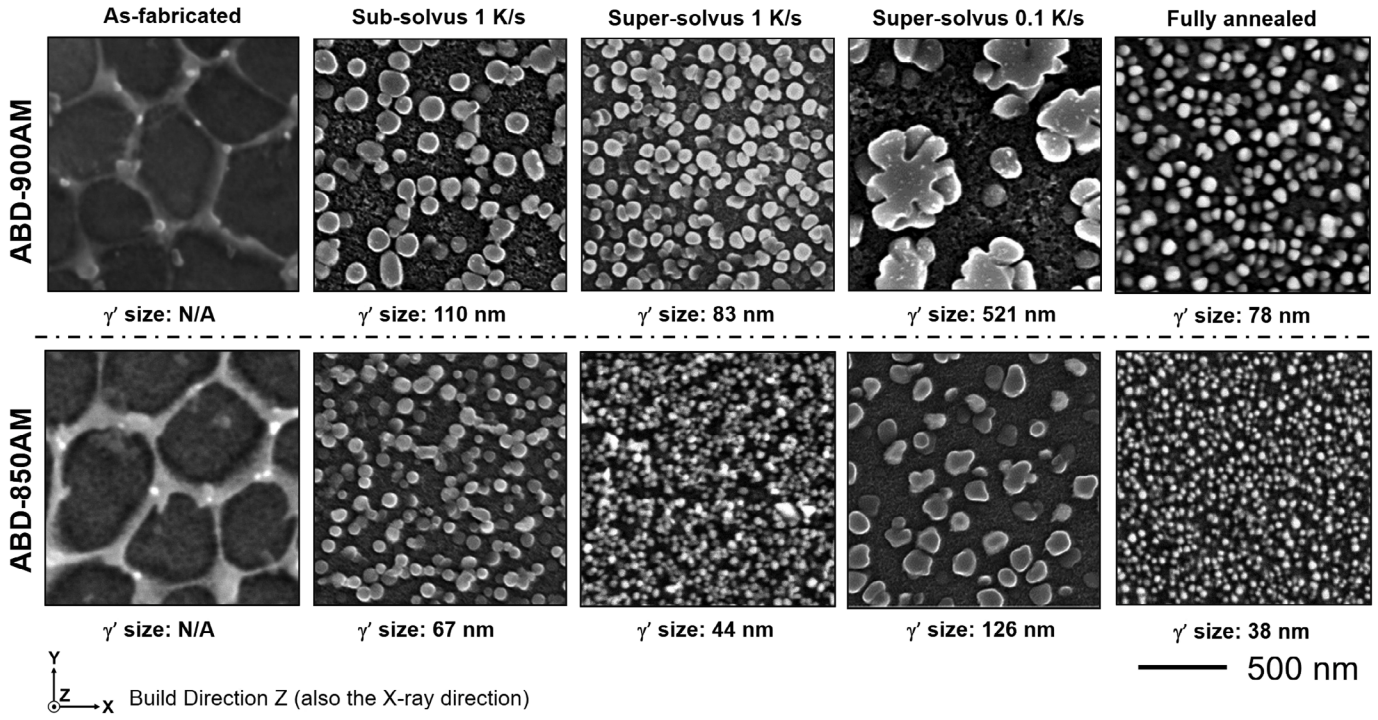


Fig. 6. γ' precipitate morphology and distribution at various heat treatment conditions for the two alloys revealed by etching. As-fabricated and fully annealed samples are also shown as reference microstructure.

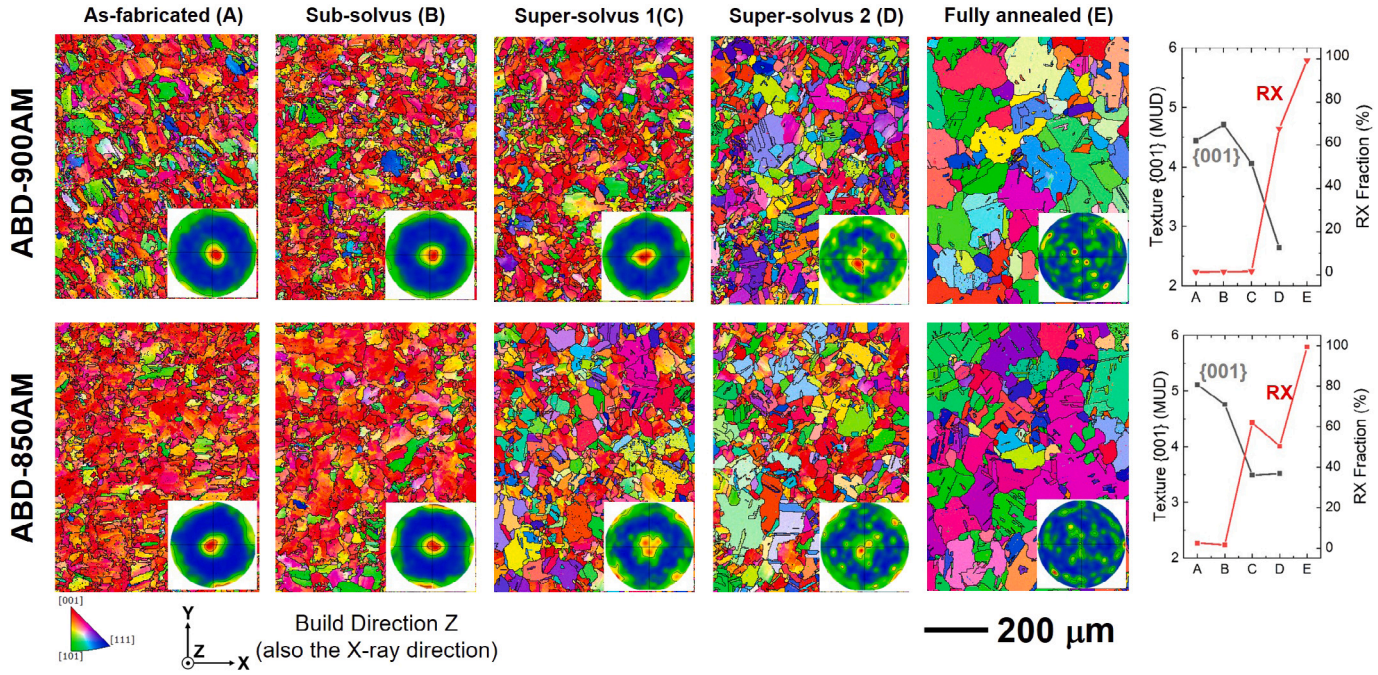


Fig. 7. Inverse pole figure (IPF) and its corresponding {0 0 1} pole figure maps viewed along the build direction (Z-axis) for both alloys at various states, including, as-fabricated, sub-solvus, super-solvus 1 & 2 and fully annealed. The corresponding {0 0 1} pole texture component and recrystallisation fraction are also shown.

S5. W is not a fast diffuser [52] making this likely to be attributed to a local heterogeneity in the chemical distribution. The volume fraction of γ' for this sample is considered small due to limited kinetics and is likely to first nucleate near cell boundaries. Furthermore, hardness testing was carried to assess the overall response of each material. Fig. 9(c) reveals a noticeable increase of Vickers hardness number of statistical significance, which strongly suggests the presence of γ' precipitation. Although residual stress redistribution can contribute to such a change in hardness number, the temperature required for a nickel superalloy to soften and subsequently relieve stress is close to, or over, 1000 °C, sometimes together with hot isostatic pressing [53]. Thus, an appreciable stress redistribution is unlikely to occur at such a

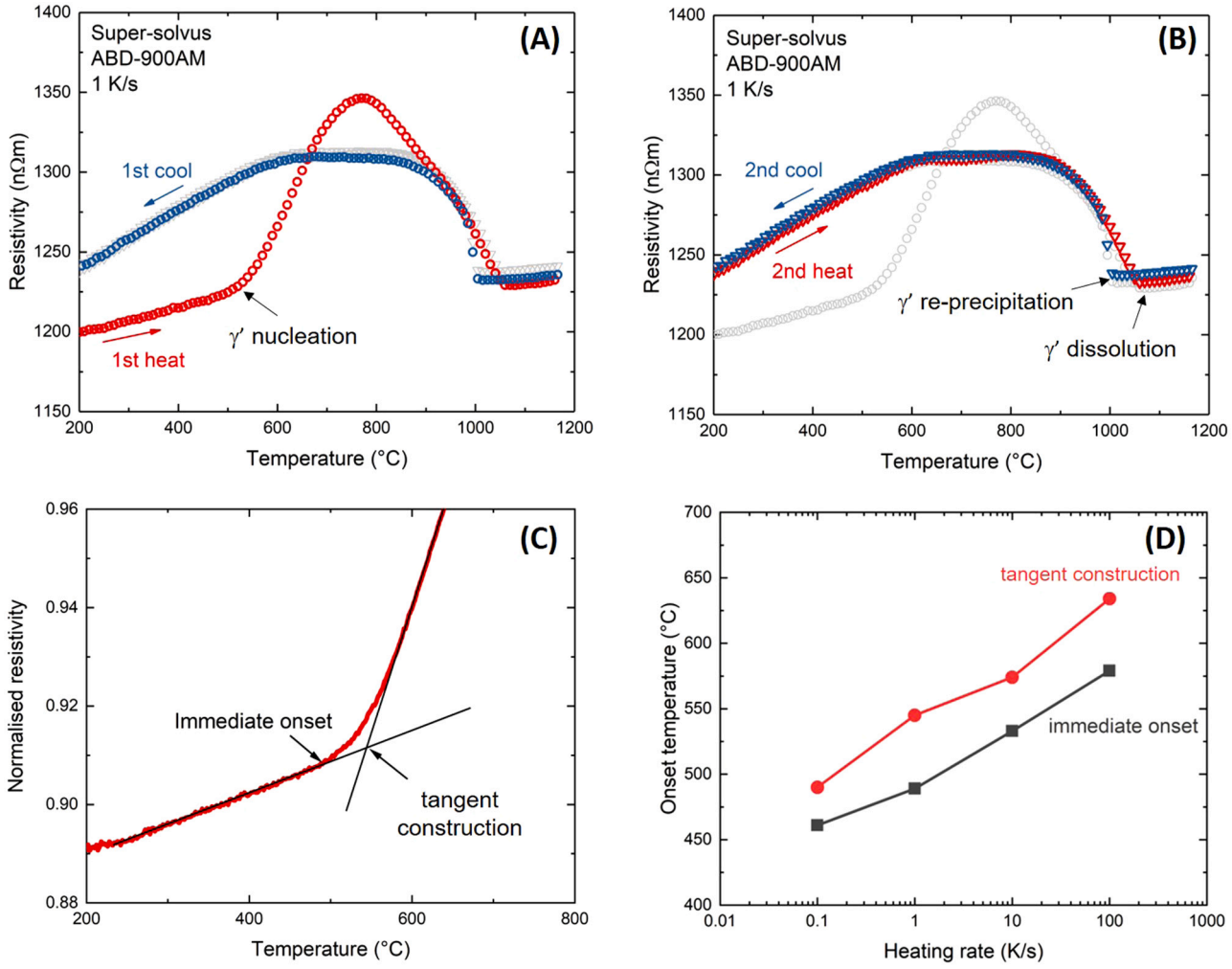


Fig. 8. (a-b) The electrical resistivity measurement are shown for the as-fabricated ABD-900AM that is heated and cooled down from super-solvus 1 temperature for two cycles. (c) demonstrates two methods of determining the first population of γ' upon heating by immediate onset and extrapolation by tangent construction. (d) illustrates the onset temperature as a function of heating rate from 10^{-1} - 10^{2} K/s with both methods.

low temperature, nor inferring a mechanical change. This is considered a manifesto of the presence of nano-metre sized precipitate embryos.

In situ monitoring of electrical resistivity (recap Fig. 8) also provides evidence for the γ/γ' reaction as early as ~450 °C, where a drastic and continuous increase of resistivity is revealed. Since γ' has a higher electrical resistance than the γ, this transition is directly attributed to the γ' formation. Additionally, the resistance value at 200 °C of the first heating cycle (1200 nΩm) has increased after the first cooling cycle (1240 nΩm). This suggests an electrical resistance difference between the supersaturated γ versus a γ/γ' mixture. Moreover, the second heating and cooling closely replicates the first cooling curve, suggesting the γ to γ' reaction occurred in a close-to-equilibrium state. Interestingly, the peak resistance on the first heating (1346 nΩm) is markedly higher than the other cycles of heating and cooling (1310 nΩm). The higher resistance during the initial heating stage is considered to be due to the first population of γ' precipitates being very small, whose domains are smaller than critical dimensions for electron scattering, as observed in other ordered systems [54,55]. In summary, the structural variation detected below or of approximately 500 °C (heating rate dependent) is attributed by the embryonic development of γ'.

4.2. Coarsening of γ' during isothermal holding

An embryonic reaction of γ/γ' at 500 °C is limited by the transformation kinetics. To study the early γ' composition, we take the precipitation to completion at 1050 °C for 2 mins and quench. This is then contrasted with a sample that was heat treated at the same temperature for 60 mins. Fig. 10(a) shows the precipitate distribution at the start and the end of an isothermal hold. Very fine precipitates (<30 nm) with cell-like structural patterns (b) have coarsened to a few hundred nm; some tertiary γ' also formed during air cooling (c). To infer the potential chemical changes during the isothermal hold, at least three APT measurements were employed for each γ/γ' mixture, i.e. quenched at the isotherm start & end (at 2 & 60 min). The quantitative dataset are presented in Table 4 and Table 5 respectively. A degree of compositional scatter between each precipitate was seen, even though some were similar in size and close in location, especially for the isothermal start sample. The γ matrix composition is used in the following analysis to interpret compositional change, assuming a perfect two phase mixture.

Fig. 11 shows the γ chemistry of the as-fabricated vs isothermally held at 1050 °C for different periods of time. In the first instance, a comparison is made between the as-fabricated and isothermally treated samples. One finds the concentration of Ti, Al, Nb & Ta (γ' formers) decreased significantly within the γ phase, whereas Cr, Co, Mo & W (solid solution elements) became more enriched, which is expected. Furthermore, when comparing between different holding times, i.e. 2 vs 60 mins, a consistent chemical change was also evident — suggesting the initial phase compositions at the isothermal start were not in equilibrium, which is consistent with similar reports elsewhere [12,

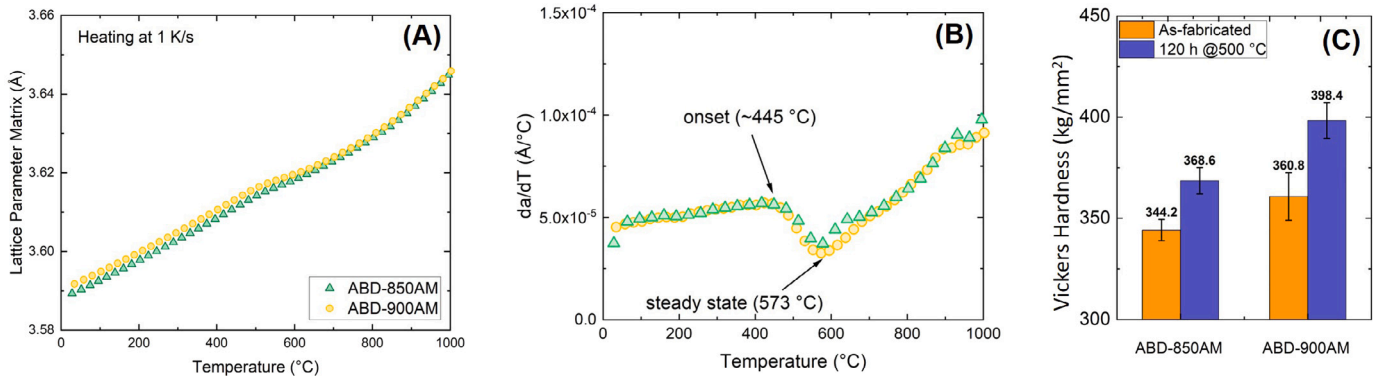


Fig. 9. Lattice parameter of the γ matrix and its first order derivative as a function of temperature for both alloys (a-b). It shows some structural change started at ~445 °C. (c) shows a comparison of Vickers hardness of the as-fabricated and 120 h exposure at 500 °C.

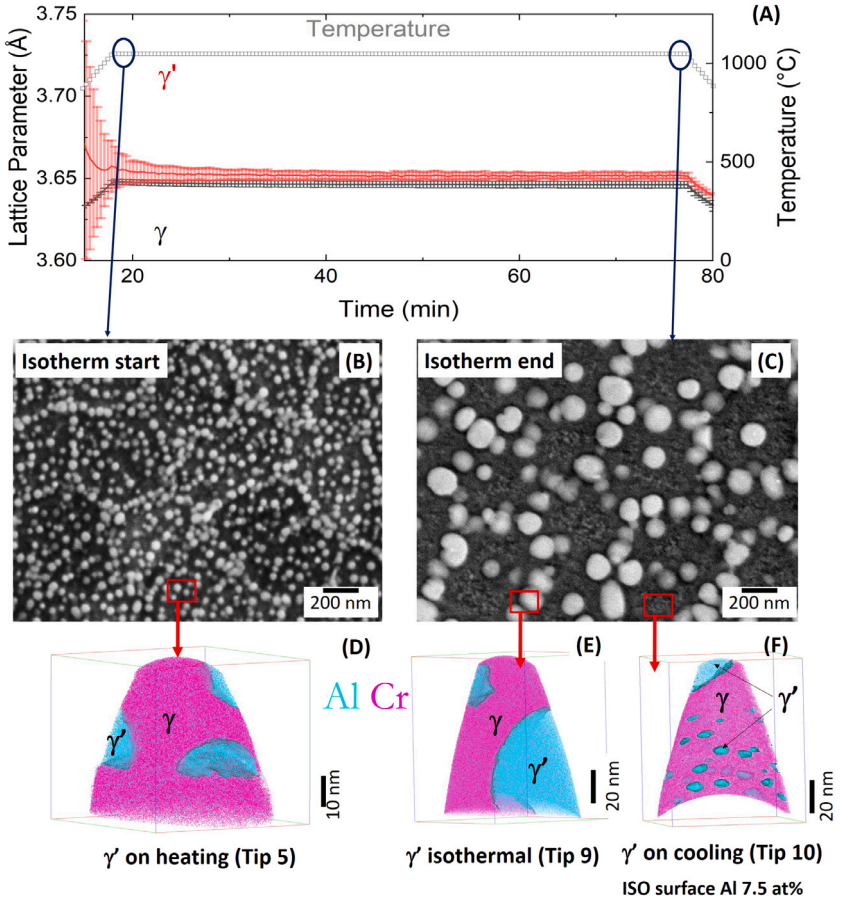


Fig. 10. Lattice parameter evolution of γ (black) and γ' (red) during isothermal treatment below solvus temperature for ABD-900AM. Microstructure at the isothermal start and end (b & c) illustrates the coarsening of precipitation via the Ostwald ripening process. APT reconstruction for γ' precipitate in each case (d-f). (For interpretation of the references to colour in this figure legend, the reader is referred to the web version of this article.)

56]. Nevertheless, the compositional evolution during holding within the γ phase is somewhat counterintuitive. As it presents, the longer isothermal hold yields a marginal enrichment of Al, Ti & Ta and a depletion of Co and Cr within the γ phase. The evidence suggests the average composition of the first γ' population has been overly concentrated by Ti, Al & Ta at the beginning, whereas the concentration decreases over time as it reaches equilibrium. CALPHAD calculation of equilibrium γ using both TCNI8 and TTNi8 databases are included for benchmark purpose in the supplementary Figure S6. It is worth noting that this trend is contradictory to conventional γ' development from the quenched samples when nanometre nuclei are available for growth [56]. However, for a super-saturated microstructure such as RR1000 powder straight after atomisation, a similar trend of elemental partitioning to our study was reported [12]. They compared heat treatment temperature at a constant time, i.e. at 900 vs 1000 °C for 15 mins, in contrast to same temperature at different time. A similar plot using their data is shown in Supplementary Figure S7 for comparison. It was concluded that the phase transformation at 900 °C for RR1000 was due to spinodal decomposition. For the current study, no definitive evidence supports this mechanism, at least for the isothermal regime. Further investigation focusing on the chemical evolution on the embryonic precipitation at approximately 700 °C is needed to rectify this.

Table 4
Composition of ABD-900AM exposed at 1050 °C for 2 min in at-% (Ni-base), measured using APT.

	Ni	Cr	Co	Al	Ti	Nb	Ta	W	Mo	C	B	Phase
Tip 5	Bal	23.79	22.35	2.97	1.50	0.53	0.25	0.98	1.41	0.127	0.010	γ
Tip 6	Bal	23.26	22.17	3.20	1.62	0.58	0.25	1.02	1.36	0.028	0.006	γ
Tip 7	Bal	22.80	21.86	3.34	1.73	0.58	0.27	1.00	1.38	0.067	0.005	γ
Tip 5	Bal	3.26	10.90	10.43	7.98	1.32	1.29	0.58	0.35	0.146	0.030	γ'
Tip 5	Bal	3.84	11.46	10.61	7.73	1.38	1.13	0.55	0.38	0.334	0.012	γ'
Tip 5	Bal	4.03	10.48	10.89	7.97	1.88	1.32	0.62	0.37	0.136	0.030	γ'
Tip 5	Bal	3.62	11.41	10.22	8.31	1.28	1.30	0.62	0.35	0.038	0.026	γ'
Tip 5	Bal	3.08	11.28	10.32	8.01	1.33	1.17	0.77	0.42	0.016	0.019	γ'
Tip 6	Bal	3.84	10.84	11.43	7.86	1.65	1.42	0.77	0.37	0.085	0.015	γ'
Tip 6	Bal	4.06	11.14	10.73	7.66	1.29	1.13	0.69	0.37	0.010	0.016	γ'
Tip 6	Bal	3.57	11.50	10.36	7.75	1.38	1.10	0.62	0.34	0.023	0.028	γ'
Tip 7	Bal	4.18	11.21	10.6	7.77	1.60	1.09	0.70	0.36	0.158	0.031	γ'
Tip 7	Bal	5.03	12.06	9.81	7.43	1.49	1.13	0.66	0.43	0.013	0.031	γ'

Table 5
Composition of ABD-900AM exposed at 1050 °C for 60 min in at-% (Ni-base), measured using APT.

	Ni	Cr	Co	Al	Ti	Nb	Ta	W	Mo	C	B	Phase	Comment
Tip 8	Bal	21.47	21.26	3.69	2.12	0.62	0.35	1.01	1.39	0.064	0.004	γ	
Tip 9	Bal	22.65	21.72	3.47	1.88	0.55	0.29	1.03	1.39	0.019	0.002	γ	
Tip 10	Bal	21.68	21.24	3.66	2.07	0.91	0.33	1.00	1.38	0.033	0.004	γ	
Tip 8	Bal	5.09	11.88	11.06	7.41	1.20	1.03	0.78	0.55	0.012	0.013	γ'	Tertiary
Tip 9	Bal	2.77	10.94	10.57	8.42	1.12	1.35	0.52	0.30	0.22	0.028	γ'	Secondary
Tip 10	Bal	2.99	11.25	10.71	8.57	2.15	1.27	0.60	0.28	0.163	0.041	γ'	Secondary
Tip 10	Bal	5.46	11.85	10.84	7.31	2.17	0.97	0.81	0.60	0.16	0.008	γ'	Tertiary
Tip 8	Bal	11.30	6.60	1.20	15.44	14.90	2.15	1.45	3.15	26.976	0.107	Carbide	

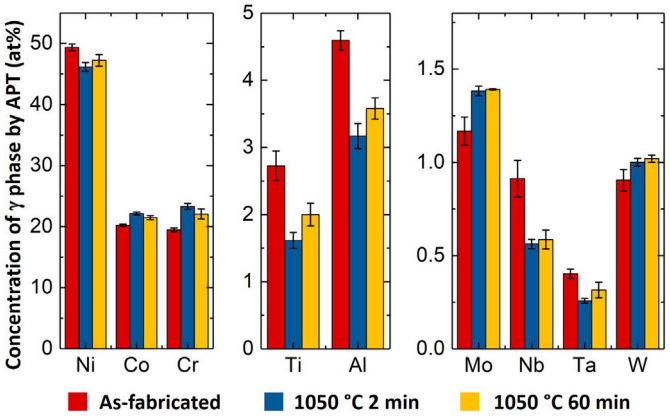


Fig. 11. Atom probe tomography analysis on elemental concentration of γ phase in three states, i.e. as-fabricated, 1050 °C for 2 & 60 mins.

The counter-intuitive compositional evolution during early γ' coarsening is considered to relate to diffusivity — the precipitation process is very likely diffusion-controlled [57]. Hargather et al. [52] obtained diffusion coefficients of dilute Ni-X alloy systems from first-principles calculation, see supplementary Figure S8 for elements relevant to this study. Although the diffusivity in their study was applied to dilute systems, the ranking of a diffusion coefficients can be used as a guide. The fastest diffusing species of interest are identified as Nb, Ta, Ti and Al throughout the temperature range (600–1200 K). These elements are between one to three orders of magnitude higher than others (Mo, Co, Cr and W). Coincidentally, the fast diffusers are all γ' formers. Thus, it is expected that these elements are of the highest mobility, which give increased local solute concentration to form clusters and eventually develop into precipitates. Pre-existing segregation along cell boundaries is expected to facilitate precipitate nucleation for a higher initial concentration, in which the cell wall is the preferred γ' location.

One anomaly in the dataset is worthy of further considerations, *i.e.* the very high lattice mismatch when precipitates initially formed upon heating. Fig. 12 shows the superlattice reflections during the heat treatment; the initial peak is extensively wide and narrows as the temperature increases. The initial peak broadening suggests the early precipitates have a wide range of compositions, corresponding to a lattice parameter range for the γ'. This also explains the scatter of initial γ' composition. As the peak narrows during the heat treatment, the composition range gets smaller. Lattice misfit is influenced by the lattice parameters, and hence solely dependent upon phase composition at a given temperature. The d-band transition metals are known to have a significant influence on γ' lattice parameters, whereby the smallest and largest positions in each period are most effective [58]. For example, Ti is more effective to induce an increase in $a_{\gamma'}$ than Cr or Co in 3d-orbital. By inferring chemical evolution between 2 vs 60 mins isothermal holding, one sees that early γ' is significantly more enriched in Ti, Al & Ta and deficient in Cr & Co – a net increase of lattice misfit is therefore expected [58]. Although it is not quantitatively proven, the exceptionally large lattice misfit during initial heating is hypothesised to be caused by the $L1_2$ lattice being overly concentrated by solutes such as Ti, Al and Ta and deficient in Cr & Co that are known to increase $a_{\gamma'}$ values.

4.3. Trigger of static recrystallisation

Recrystallisation is a key phenomenon in metal processing via hot deformation, which is used to control grain size and texture to deliver desirable properties, such as the strength and ductility synergy [59]. Recently, it has been shown that recrystallisation can happen in some nickel superalloys with no prior external deformation applied [22,60]. Here, the additive manufacturing process generated significant strain at the crystal level, due to the extreme thermal gradients [61].

The GND density for the AM microstructure exhibits a very unique bimodal distribution [10]. The formation of local level heterogeneous dislocation level is considered due to uneven spread of dislocation trapping sites at cell intercellular particles, such as carbides, borides and oxides. The thermal induced dislocations are pinned more in a region with higher pinning sites resulting in some areas obtaining a higher dislocation density than others. Its evolution during the heat treatment cycle studied in the synchrotron experiment has been characterised using HR-EBSD, see Fig. 13(a-b). The GND density map can be used to identify the recrystallised and unrecrystallised regions — the low

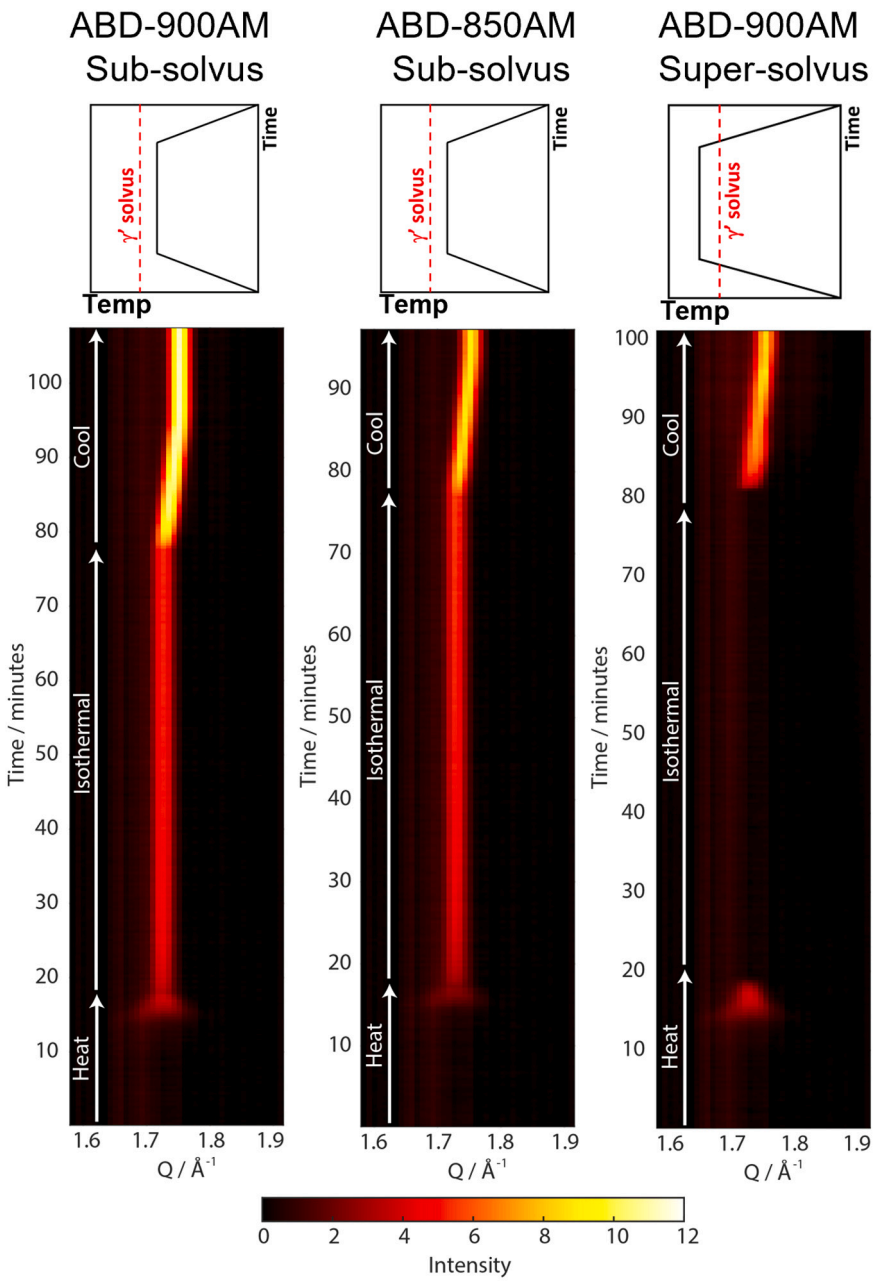


Fig. 12. Evolution of {001} superlattice reflection as a function of time for ABD-900AM and ABD-850AM for sub-solvus and super-solvus 1 heat treatments.

GND density region (dark blue), suggesting recrystallisation is complete and the rest remains unchanged. The evolution of the GND density observed in the histogram can be used to interpret its corresponding microstructural change. For example in Fig. 10(c), where a trimodal distribution is overlaid on top of the as-fabricated state. Both medium and high GND regions (ρ = 10^{14} & $10^{14.8}$ m^{-2}) have encountered recrystallisation and transformed to the low GND region (ρ = 10^{13} m^{-2}). Clearly, the high GND region in the microstructure is likely to trigger recrystallisation.

The time for recrystallisation to start is considered here; whilst the onset of recrystallisation cannot be measured directly from the diffraction data, rapid grain growth can indeed be detected. As grains grow, large crystals in the Bragg condition diffract strongly and their diffraction spots can be seen, in contrast to the continuous diffraction rings observed earlier in the tests (due to a fine grain distribution). As soon as any spottiness appears in the diffraction patterns, significant grain growth must be active, which have followed recrystallisation. The sequence of diffraction pattern obtained from ABD-900AM was checked in this way, where two areas of interests are shown in Fig. 14, in blue and yellow boxes. Evidently, the first tiny spot was detected in the blue region after 5 min of isothermal holding, which then evolved into much higher intensity spots at the end of the dwell time (60 min). Furthermore, the first spot at the blue region has shifted its position, suggesting crystal rotation during recrystallisation. It was observed that some diffraction spots appeared, then disappeared. Either this grain was consumed during the grain growth, or the grain itself underwent a rotation, and moved out of the diffraction condition. The latter may be possible if significant residual stresses of this or neighbouring grains are relieved during the heat treatment.

The recrystallisation temperature for ABD-900AM is high; a heat treatment at 1220 °C did show evidence of the recrystallisation process, but 1165 °C did not. The recrystallisation onset window is therefore in this range. It is worth noting that the recrystallisation start temperature is significantly higher than most superalloys from traditional hot

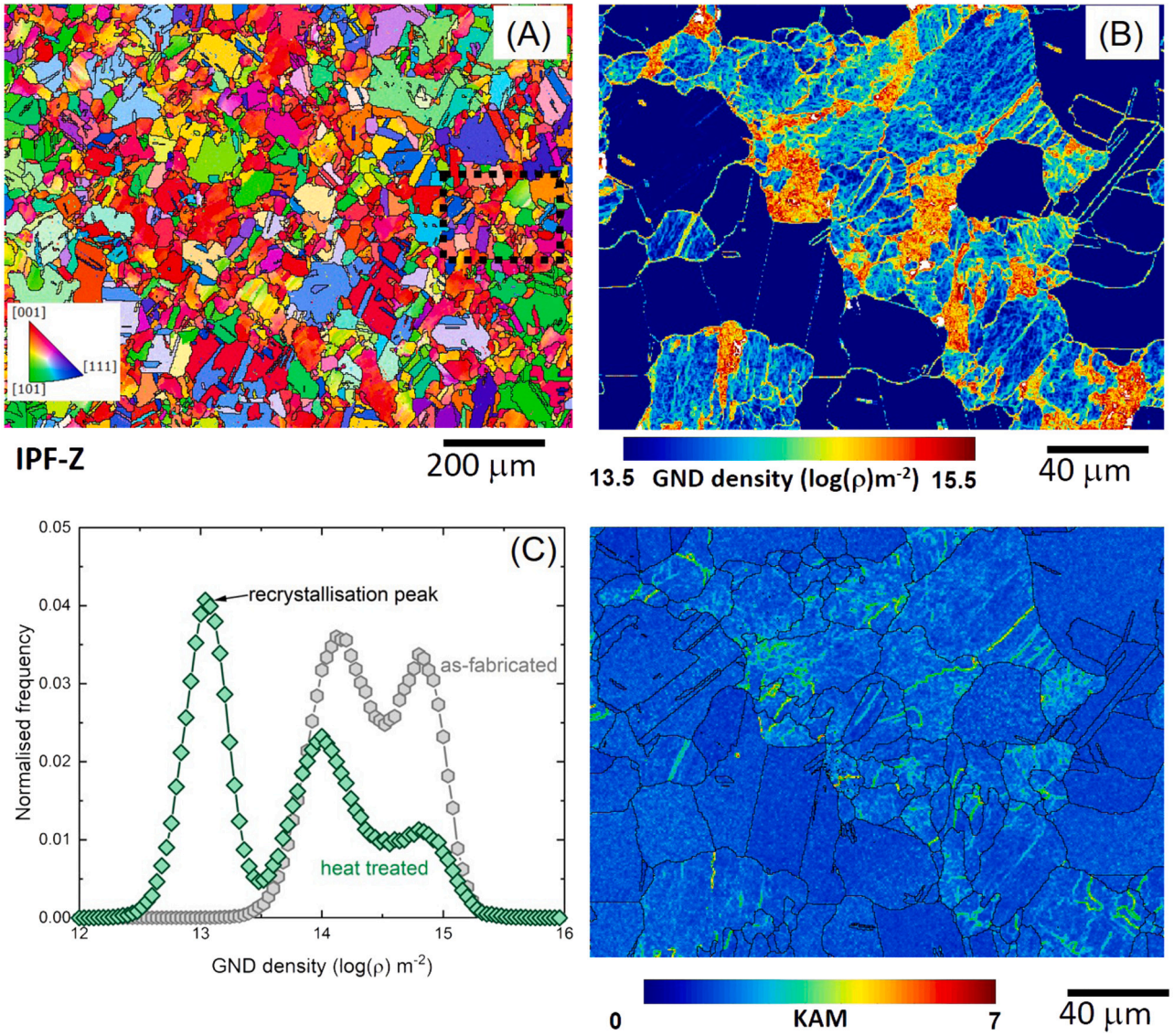


Fig. 13. Microstructure of ABD-850AM after super-solvus 1 heat treatment that demonstrated static recrystallisation. (a) inverse pole figure along the build direction (Z-axis), (b) GND density map of a magnified region of interest and (c) a trimodal distribution of GND histogram of the sample in comparison to a bimodal distribution in as-fabricated state [10].

deformation, usually within ~850-950 °C or below, such as IN625, [62] IN718 [63], Waspaloy [64] and C&W M647 [65]. In addition, it is also much higher than many other AM reports where slightly higher than γ' solvus is sufficient [66,67], possibly due to powder reuse. The root cause for requiring a very high onset temperature is considered to be a fine dispersion of alumina oxide and MC carbides along the cell and grain boundaries while the solidification process occurred – these phases can provide a strong Zener-type pinning effect [68]. The presence of fine alumina oxide could link to oxygen intake of the recycled metal powder [69,70].

5. Implications to heat treatment for AM superalloys

This body of work has identified a sequence of microstructure development at various stages of the heat treatment process for two nickel-based superalloys. Whilst the experimental evidence was focussed on the L-PBF processing, some general insights and directions are relevant to the design of heat treatment regardless. One realises the starting microstructure is homogeneous on the micro-scale; it is no longer necessary to re-solutionise the microstructure if sub-micron to nano-metre scale segregation is acceptable. In addition, should a full solutioning be essential, a much reduced holding time will be required due to the much shorter diffusion distance in comparison to conventional casting. Moreover, the γ' distribution will be determined during the heating step, where it shows sensitivity to the associated heating rate. Controlled heating during precipitation reactions warrants a comprehensive study; it is just as important as controlled cooling from solution treatment for conventional superalloys [48,71]. It is anticipated that for a sub-solvus heat treatment, the heating rate may have a significant effect on the mechanical performance as it controls the γ' size and distribution. The reduction of anisotropy and dislocation densities can be achieved *via* a very high temperature isothermal heat treatment, going merely beyond the γ' solvus may not be sufficient and is deemed to be sensitive to the processing conditions as well. The onset of static recrystallisation occurs within minutes, whereas it takes hours for the material to achieve full recrystallisation. The resultant microstructure with reduced anisotropy and larger grain sizes, nevertheless, faces a universal ductility challenge as evidenced in multiple superalloy systems [13,72–75]. Future work to understand the root cause of the embrittlement and strategies for mitigation is needed.

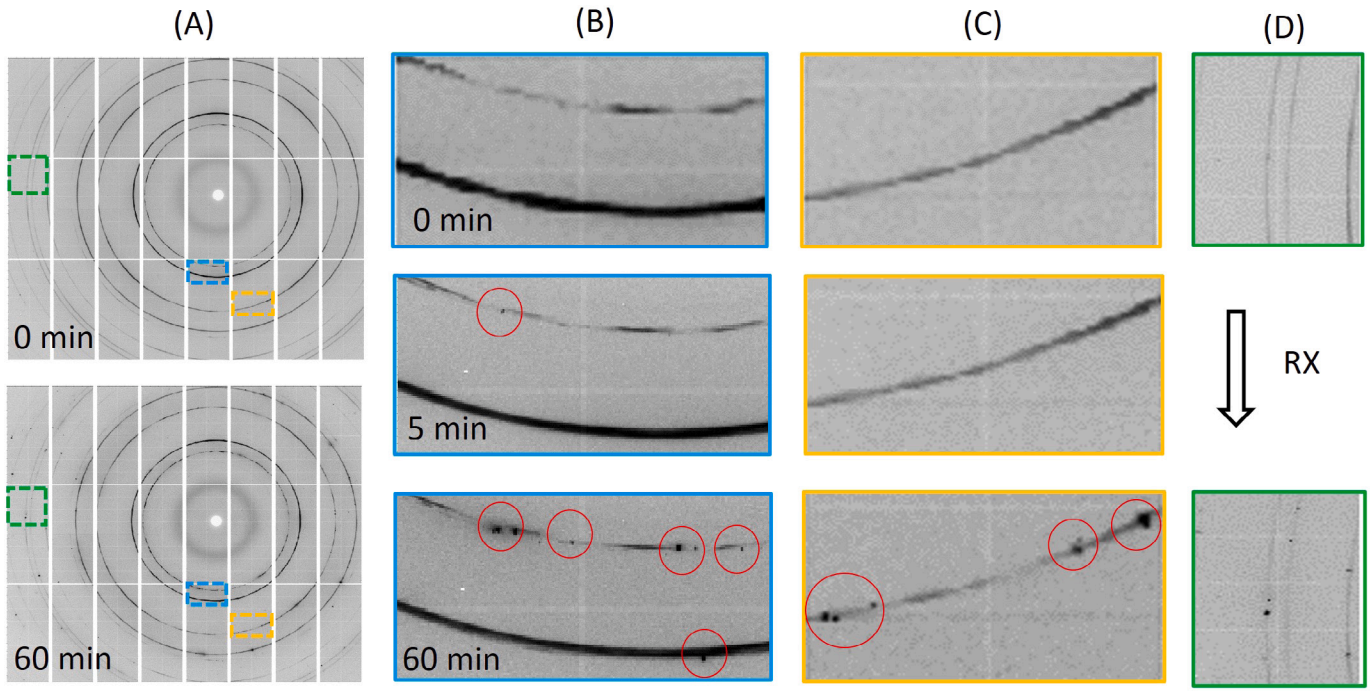


Fig. 14. Evolution of synchrotron diffraction patterns of ABD-900AM, at a supersolvus temperature, during recrystallisation. The initially continuous diffraction patterns develop isolated diffraction spots after 5 mins, indicative of grain growth.

6. Summary and conclusions

A comprehensive and holistic study was performed on the effect of heat treatment on microstructure evolution in two novel nickel-based superalloys which were designed specifically for additive manufacturing [10]. A combination of *in situ* and *ex situ* techniques across multiple length-scale has been employed to study the as-fabricated microstructure as a baseline and to interrogate the γ/γ' reaction and static recrystallisation behaviour. The as-fabricated microstructure from L-PBF consists of a super-saturated γ-matrix. The non-equilibrium microstructure is devoid of γ' precipitates, remnant from the rapid cyclic heating and cooling during fabrication. Significant insights have been gleaned into the transformation kinetics and non-equilibrium structural evolution during the different stages of these practically-relevant heat treatments. The following specific conclusions can be drawn from the work:

1. Pre-existing segregation is detected in the as-fabricated state for Ti at cellular boundaries, although the level is not severe. Trace elements such as C and B also reside frequently at cell boundaries. Elemental segregation of C is not observed, found only in particles suggesting carbides, whereas B exhibits both segregation and particles.
2. Upon the first heating cycle, the first population of γ' precipitates forms preferentially along cell boundaries. For ABD-900AM, it becomes detectable below 500 °C. The diffusion-assisted transformation is highly sensitive to the heating rate: the γ' onset temperature detected varies between 461 °C at 0.1 K/s to 579 °C at 100 K/s.
3. The kinetics of γ' evolution upon heating is very sluggish initially until rapid transformation takes place at 740 °C for ABD-900AM and 824 °C for ABD-850AM. Direct evidence is presented of the precipitation rate accelerating to a maximum and reaching its first peak in volume fraction. The fraction decreases with further heating or else stagnates to a constant value during isothermal holding.
4. The lattice parameter for the initial γ' formed upon heating is exceptionally large, contributing to a significant positive lattice mismatch of $\sim 25 \times 10^{-3}$. As heat treatment progresses, the lattice misfit decreases by an order of magnitude as the system moves towards equilibrium.
5. Atom probe tomography reveals the phase compositions vary greatly between the non-equilibrium and equilibrium state. The initial γ' is more depleted in Co and Cr, and enriched in Ti, Al, Nb, Ta, Mo and W. The initial large lattice parameter of precipitates is considered to associate with the non-equilibrium chemical composition.
6. Static recrystallisation can occur in the as-fabricated microstructure despite the absence of prior deformation; it is sensitive to the temperature of the isothermal heat treatment. It is driven by the consumption of the local dislocations; the texture strength in the as-fabricated condition is significantly reduced and is accompanied by notable grain growth, which occurs within minutes.

CRediT authorship contribution statement

Yuanbo T. Tang: Conceptualization, Writing – original draft, Writing – review & editing, Investigation, Funding acquisition, Formal analysis, Data curation. **Chinnapat Panwisawas:** Writing – review & editing, Funding acquisition, Data curation, Conceptualization. **Benjamin M. Jenkins:** Writing – review & editing, Investigation, Formal analysis, Data curation. **Junliang Liu:** Investigation, Formal analysis, Data curation. **Zhao Shen:** Writing – review & editing, Investigation, Formal analysis, Data curation. **Enrico Salvati:** Writing – review & editing, Investigation, Formal analysis, Data curation, Conceptualization. **Yilun Gong:** Writing – review & editing, Investigation. **Joseph N. Ghoussoub:** Writing – review & editing, Investigation. **Stefan Michalik:** Writing – review & editing, Methodology, Formal analysis, Data curation. **Bryan Roebuck:** Methodology, Formal analysis, Data curation. **Paul A.J. Bagot:** Resources, Project administration. **Sergio Lozano-Perez:** Writing – review & editing, Methodology, Investigation, Formal analysis, Data curation. **Chris R.M. Grovenor:** Writing – review

& editing, Methodology, Formal analysis. **Michael P. Moody:** Writing – review & editing, Methodology, Investigation, Formal analysis. **Alexander M. Korsunsky:** Writing – review & editing, Investigation, Funding acquisition, Formal analysis, Data curation, Conceptualization. **David M. Collins:** Writing – review & editing, Methodology, Investigation, Funding acquisition, Formal analysis, Data curation, Conceptualization. **Roger C. Reed:** Writing – review & editing, Supervision, Investigation, Funding acquisition, Formal analysis, Conceptualization.

Declaration of competing interest

The authors declare that they have no known competing financial interests or personal relationships that could have appeared to influence the work reported in this paper.

Data availability

Data will be made available on request.

Acknowledgements

The authors acknowledge funding from Innovate UK, formerly the Technology Strategy Board (TSB), under project number 104047. The authors also appreciate the beam time allocated to them under award MG23674 at the Diamond Light Source (UK). YTT and RCR are grateful for Alloyed Ltd for provision of materials. YTT and RCR acknowledge support from the Henry Royce Institute for Advanced Materials, funded through EPSRC grants (EP/R00661X/1) and (EP/X527257/1). The authors acknowledge use of characterisation facilities, alongside financial support provided by the Henry Royce Institute (Grant ref EP/R010145/1) and byEPSRC through the Strategic Equipment Fund, grant EP/N010868/1. The atom probe facilities at the University of Oxford are funded by the EPSRC (EP/M022803/1). BMJ, JL and CRMG acknowledges support from EPSRC programme grant MIDAS (EP/S01702X/1). BMJ is a recipient of the WINNINGNormandy Program supported by the Normandy Region and would like to acknowledge this project has received funding from the European Union's Horizon 2020 research and innovation programme under the Marie Sklodowska Curie grant agreement No. 101034329. YTT and CP acknowledge the funding from Innovation Fellowship by Engineering and Physical Science Research Council (EPSRC), UK Research and Innovation (UKRI) (grant number: EP/S000828/2). YTT acknowledges discussions with Prof D.G. McCartney and Dr S. Utada.

Appendix A. Supplementary data

Supplementary material related to this article can be found online at https://doi.org/10.1016/j.addma.2023.103389.

References

[1] R.C. Reed, The Superalloys: Fundamentals and Applications, Cambridge University Press, 2006.
[2] T.M. Pollock, Alloy design for aircraft engines, Nature Mater. 15 (2016) 809–815.
[3] M.J. Donachie, S.J. Donachie, Superalloys: A Technical Guide, ASM International, 2002.
[4] C.T. Sims, N.S. Stoloff, W.C. Hagel, Superalloys II.: High-Temperature Materials for Aerospace and Industrial Power, John Wiley & Sons, Inc. 1987.
[5] S.A. Tofail, E.P. Koumoulos, A. Bandyopadhyay, S. Bose, L. O'Donoghue, C. Charitidis, Additive manufacturing: scientific and technological challenges, market uptake and opportunities, Mater. Today 21 (1) (2018) 22–37.
[6] C. Körner, Additive manufacturing of metallic components by selective electron beam melting — A review, Int. Mater. Rev. 61 (5) (2016) 361–377.
[7] C. Panwisawas, Y.T. Tang, R.C. Reed, Metal 3D printing as a disruptive technology for superalloys, Nature Commun. 11 (2327) (2020).
[8] J. Pistor, S. Hagen, S. Virtanen, C. Körner, Influence of the microstructural homogeneity on the high-temperature oxidation behavior of a single crystalline Ni-base superalloy, Scr. Mater. 207 (2022) 114301.
[9] D. Herzog, V. Seyda, E. Wycisk, C. Emmelmann, Additive manufacturing of metals, Acta Mater. 117 (2016) 371–392.
[10] Y.T. Tang, C. Panwisawas, J.N. Ghoussoub, Y. Gong, J.W.G. Clark, A.A.N. Németh, D.G. McCartney, R.C. Reed, Alloys-by-design: Application to new superalloys for additive manufacturing, Acta Mater. 202 (2021) 417–436.
[11] P.A. Hooper, Melt pool temperature and cooling rates in laser powder bed fusion, Addit. Manuf. 22 (2018) 548–559.
[12] D.M. Collins, N. D'Souza, C. Panwisawas, C. Papadaki, G.D. West, A. Kostka, P. Kontis, Spinodal decomposition versus classical γ' nucleation in a nickel-base superalloy powder: An in-situ neutron diffraction and atomic-scale analysis, Acta Mater. 200 (2020) 959–970.
[13] Y.T. Tang, J.N. Ghoussoub, C. Panwisawas, D.M. Collins, S. Amirkhanlou, J.W.G. Clark, A.A.N. Németh, D. Graham McCartney, R.C. Reed, The effect of heat treatment on tensile yielding response of the new superalloy ABD-900AM for additive manufacturing, in: S. Tin, M. Hardy, J. Clews, J. Cormier, Q. Feng, J. Marcin, C. O'Brien, A. Suzuki (Eds.), Superalloys 2020, Springer International Publishing, Cham, 2020, pp. 1055–1065.
[14] J. Xu, P. Kontis, R.L. Peng, J. Moverare, Modelling of additive manufacturability of nickel-based superalloys for laser powder bed fusion, Acta Mater. 240 (2022) 118307.
[15] V. Divya, R. Muñoz-Moreno, O. Messé, J. Barnard, S. Baker, T. Illston, H. Stone, Microstructure of selective laser melted CM247LC nickel-based superalloy and its evolution through heat treatment, Mater. Charact. 114 (2016) 62–74.
[16] X. Wang, L.N. Carter, B. Pang, M.M. Attallah, M.H. Loretto, Microstructure and yield strength of SLM-fabricated CM247LC Ni-superalloy, Acta Mater. 128 (2017) 87–95.
[17] J. Xu, H. Gruber, R. Lin Peng, J. Moverare, A novel γ' strengthened nickel-based superalloy for laser powder bed fusion, Materials 13 (21) (2020).
[18] C. Kenel, A. De Luca, S.S. Joglekar, C. Leinenbach, D.C. Dunand, Evolution of Y_2O_3 dispersoids during laser powder bed fusion of oxide dispersion strengthened Ni-Cr-Al-Ti γ/γ' superalloy, Addit. Manuf. 47 (2021) 102224.
[19] L. Haußmann, S. Neumeier, M. Kolb, J. Ast, G. Mohanty, J. Michler, M. Göken, Local mechanical properties at the dendrite scale of Ni-based superalloys studied by advanced high temperature indentation creep and micropillar compression tests, in: S. Tin, M. Hardy, J. Clews, J. Cormier, Q. Feng, J. Marcin, C. O'Brien, A. Suzuki (Eds.), Superalloys 2020, Springer International Publishing, 2020, pp. 273–281.
[20] Y.-L. Kuo, S. Horikawa, K. Kakehi, Effects of build direction and heat treatment on creep properties of Ni-base superalloy built up by additive manufacturing, Scr. Mater. 129 (2017) 74–78.
[21] K. Chen, R. Huang, Y. Li, S. Lin, W. Zhu, N. Manura, J. Li, Z.-W. Shan, E. Ma, Rafting-enabled recovery avoids recrystallization in 3D-printing-repaired single-crystal superalloys, Adv. Mater. 32 (12) (2020) 1907164.
[22] R. Munoz-Moreno, V. Divya, S. Driver, O. Messe, T. Illston, S. Baker, M. Carpenter, H. Stone, Effect of heat treatment on the microstructure, texture and elastic anisotropy of the nickel-based superalloy CM247LC processed by selective laser melting, Mater. Sci. Eng. A 674 (2016) 529–539.
[23] I. Waugh, E. Moore, A. Greig, J. Macfarlane, W. Dick-Cleland, Additive manufacture of rocket engine combustion chambers using the ABD-900AM nickel superalloy, in: Space Propulsion 2020+1, 2021.
[24] J. Ghoussoub, Y. Tang, W. Dick-Cleland, A. Nemeth, Y. Gong, D. McCartney, A. Cocks, R. Reed, On the influence of alloy composition on the additive manufacturability of Ni-based superalloys, Metall. Mater. Trans. A 53 (2022) 962–983.
[25] M. Drakopoulos, T. Connolley, C. Reinhard, R. Atwood, O. Magdysyuk, N. Vo, M. Hart, L. Connor, B. Humphreys, G. Howell, S. Davies, T. Hill, G. Wilkin, U. Pedersen, A. Foster, N.D. Maio, M. Basham, F. Yuan, K. Wanelik, I12: the joint engineering, environment and processing (JEEP) beamline at diamond light source, J. Synchrotron Radiat. 22 (2015) 828–838.
[26] D. Collins, D. Crudden, E. Alabort, T. Connolley, R. Reed, Time-resolved synchrotron diffractometry of phase transformations in high strength nickel-based superalloys, Acta Mater. 94 (2015) 244–256.
[27] M.L. Hart, M. Drakopoulos, C. Reinhard, T. Connolley, Complete elliptical ring geometry provides energy and instrument calibration for synchrotron-based two-dimensional X-ray diffraction, J. Appl. Crystallogr. 46 (2013) 1249–1260.
[28] M. Basham, J. Filik, M.T. Wharmby, P.C.Y. Chang, B.E. Kassaby, M. Gerring, J. Aishima, K. Levik, B.C.A. Pulford, I. Sikharulidze, D. Sneddon, M. Webber, S.S. Dhesi, F. Maccherozzi, O. Svensson, S. Brockhauser, A.W.A. G. Naray, Data analysis WorkbeNch (DAWN), J. Synchrotron Radiat. 22 (2015) 853–858.
[29] J. Filik, A.W. Ashton, P.C.Y. Chang, P.A. Chater, S.J. Day, M. Drakopoulos, M.W. Gerring, M.L. Hart, O.V. Magdysyuk, S. Michalik, A. Smith, C.C. Tang, N.J. Terrill, M.T. Wharmby, H. Wilhelm, Processing two-dimensional X-ray diffraction and small-angle scattering data in DAWN 2, J. Appl. Crystallogr. 50 (2017) 959–966.
[30] H. Stone, T. Holden, R. Reed, On the generation of microstrains during the plastic deformation of Waspaloy, Acta Mater. 47 (17) (1999) 4435–4448.
[31] S. Sulzer, E. Alabort, A. Németh, B. Roebuck, R. Reed, On the rapid assessment of mechanical behavior of a prototype nickel-based superalloy using small-scale testing, Metall. Mater. Trans. A 49 (2018) 4214–4235.
[32] B. Roebuck, D.C. Cox, R.C. Reed, An innovative device for the mechnical testing of miniature specimens of superalloys, in: K.A. Green, T.M. Pollock, H. Harada, T.E. Howson, R.C. Reed, J.J. Schirra, S. Walston (Eds.), Superalloys 2004, The Minerals, Metals & Materials Society, 2004, pp. 523–528.

[33] B. Roebuck, D. Cox, R. Reed, The temperature dependence of γ' volume fraction in a Ni-based single crystal superalloy from resistivity measurements, Scr. Mater. 44 (6) (2001) 917–921.

[34] S. Utada, R. Sasaki, R.C. Reed, Y.T. Tang, In-situ monitoring of phase transition and microstructure evolution in Ni-based superalloys by electrical resistivity: Direct comparison with differential scanning calorimetry and application to case studies, Metall. Mater. Trans. A (2023) in print.

[35] A.J. Wilkinson, G. Meaden, D.J. Dingley, High-resolution elastic strain measurement from electron backscatter diffraction patterns: New levels of sensitivity, Ultramicroscopy 106 (4) (2006) 307–313.

[36] T. Britton, A.J. Wilkinson, High resolution electron backscatter diffraction measurements of elastic strain variations in the presence of larger lattice rotations, Ultramicroscopy 114 (2012) 82–95.

[37] A.J. Wilkinson, D. Randman, Determination of elastic strain fields and geometrically necessary dislocation distributions near nanoindents using electron back scatter diffraction, Phil. Mag. 90 (9) (2010) 1159–1177.

[38] M. Miller, K. Russell, Atom probe specimen preparation with a dual beam SEM/FIB miller, Ultramicroscopy 107 (9) (2007) 761–766.

[39] K. Thompson, D. Lawrence, D. Larson, J. Olson, T. Kelly, B. Gorman, In situ site-specific specimen preparation for atom probe tomography, Ultramicroscopy 107 (2) (2007) 131–139.

[40] J. Liu, K. Li, J. Sayers, T. Aarholt, G. He, H. Hulme, A. Garner, M. Preuss, H. Nordin, J.M. Partezana, M. Limback, S. Lozano-Perez, S. Ortner, C.R. Grovenor, Characterisation of deuterium distributions in corroded zirconium alloys using high-resolution SIMS imaging, Acta Mater. 200 (2020) 581–596.

[41] M. Kirka, K. Unocic, N. Raghavan, F. Medina, R. Dehoff, S. Babu, Microstructure development in electron beam-melted inconel 718 and associated tensile properties, JOM 68 (2016) 1012–1020.

[42] T. McAuliffe, I. Bantounas, L. Reynolds, A. Foden, M. Hardy, T. Britton, D. Dye, Quantitative precipitate classification and grain boundary property control in Co/Ni-base superalloys, Metall. Mater. Trans. A 52 (2021) 1649–1664.

[43] V.A. Vorontsov, T.P. McAuliffe, M.C. Hardy, D. Dye, I. Bantounas, Precipitate dissolution during deformation induced twin thickening in a CoNi-base superalloy subject to creep, Acta Mater. 232 (2022) 117936.

[44] A. Després, S. Antonov, C. Mayer, C. Tassin, M. Veron, J.-J. Blandin, P. Kontis, G. Martin, On the role of boron, carbon and zirconium on hot cracking and creep resistance of an additively manufactured polycrystalline superalloy, Materialia 19 (2021) 101193.

[45] S. Huang, K. An, Y. Gao, A. Suzuki, Determination of γ/γ' lattice misfit in Ni-based single crystal superalloys at high temperatures by neutron diffraction, Metall. Mater. Trans. A 49A (2018) 740–751.

[46] L. Dirand, J. Cormier, A. Jacques, J.-P. Chateau-Cornu, T. Schenk, O. Ferry, P. Bastie, Measurement of the effective γ/γ' lattice mismatch during high temperature creep of Ni-based single crystal superalloy, Mater. Charact. 77 (2013) 32–46.

[47] A. Heckl, S. Neumeier, M. Göken, R. Singer, The effect of re and ru on γ/γ' microstructure, γ-solid solution strengthening and creep strength in nickel-base superalloys, Mater. Sci. Eng. A 528 (9) (2011) 3435–3444.

[48] R.J. Mitchell, M. Hardy, M. Preuss, S. Tin, Development of γ' morphology in a P/M rotor disc alloys during heat treatment, in: Superalloys 2004, 2004, pp. 361–370,

[49] C. Papadaki, W. Li, A.M. Korsunsky, On the dependence of γ' precipitate size in a nickel-based superalloy on the cooling rate from super-solvus temperature heat treatment, Materials 11 (9) (2018).

[50] Y.T. Tang, N. D'Souza, B. Roebuck, P. Karamched, C. Panwisawas, D.M. Collins, Ultra-high temperature deformation in a single crystal superalloy: Mesoscale process simulation and micromechanisms, Acta Mater. 203 (2021) 116468.

[51] W. Boettinger, U. Kattner, K. Moon, J. Perepezko, DTA and Heat Flux DSC Measurements of Alloy Melting and Freezing, National Institute of Standards and Technology Special Publication, 2006, pp. 151–221.

[52] C.Z. Hargather, S.-L. Shang, Z.-K. Liu, A comprehensive first-principles study of solute elements in dilute Ni alloys: Diffusion coefficients and their implications to tailor creep rate, Acta Mater. 157 (2018) 126–141.

[53] T. DebRoy, H. Wei, J. Zuback, T. Mukherjee, J. Elmer, J. Milewski, A. Beese, A. Wilson-Heid, A. De, W. Zhang, Additive manufacturing of metallic components – process, structure and properties, Prog. Mater. Sci. 92 (2018) 112–224.

[54] B. Noble, G.E. Thompson, Precipitation characteristics of aluminium-lithium alloys, Met. Sci. J. 5 (1) (1971) 114–120.

[55] B. Noble, S. Bray, On the α(Al)/δ'(Al_3Li) metastable solvus in aluminium-lithium alloys, Acta Mater. 46 (17) (1998) 6163–6171.

[56] T. Rojhirunsakool, A. Singh, S. Nag, J. Hwang, J. Tiley, R. Banerjee, Temporal evolution of non-equilibrium γ' precipitates in a rapidly quenched nickel base superalloy, Intermetallics 54 (2014) 218–224.

[57] A. Mottura, N. Warnken, M. Miller, M. Finnis, R. Reed, Atom probe tomography analysis of the distribution of rhenium in nickel alloys, Acta Mater. 58 (3) (2010) 931–942.

[58] J.D. Allen, Effect of Chemistry and Temperatureon Planar Defects in Superalloys (Ph.D. thesis), University of Birmingham, 2019.

[59] C. Zhang, Q. Yu, Y.T. Tang, M. Xu, H. Wang, C. Zhu, J. Ell, S. Zhao, B.E. MacDonald, P. Cao, J.M. Schoenung, K.S. Vecchio, R.C. Reed, R.O. Ritchie, E.J. Lavernia, Strong and ductile FeNiCoAl-based high-entropy alloys for cryogenic to elevated temperature multifunctional applications, Acta Mater. 242 (2023) 118449.

[60] N. Kouraytem, J. Varga, B. Amin-Ahmadi, H. Mirmohammad, R.A. Chanut, A.D. Spear, O.T. Kingstedt, A recrystallization heat-treatment to reduce deformation anisotropy of additively manufactured Inconel 718, Mater. Des. 198 (2021) 109228.

[61] W.J. Sames, F.A. List, S. Pannala, R.R. Dehoff, S.S. Babu, The metallurgy and processing science of metal additive manufacturing, Int. Mater. Rev. 61 (5) (2016) 315–360.

[62] Z. Jia, Z. Gao, J. Ji, D. Liu, T. Guo, Y. Ding, Study of the dynamic recrystallization process of the Inconel625 alloy at a high strain rate, Materials 12 (510) (2019).

[63] R. Singh, J. Hyzak, T. Howson, R. Biederman, Recrystallization behavior of cold rolled alloy 718, in: E.A. Loria (Ed.), Superalloys 718, 625 and Various Derivatives, The Minerals, Metals & Materials Society, 1991, pp. 205–215.

[64] A. Guimaraes, J. Jonas, Recrystallization and aging effects associated with the high temperature deformation of waspaloy and inconel 718, Metall. Mater. Trans. A 12 (1981).

[65] F. Adziman, R. Takai, Y.T. Tang, S. Ishikawa, D. Barba, E. Alabort, A. Nemeth, N. Kanno, R. Reed, On optimising ring-rolling manufacturability of C&W Nickel superalloys for aero-engine turbine disc, in: S. Tin, M. Hardy, J. Clews, J. Cormier, Q. Feng, J. Marcin, C. O'Brien, A. Suzuki (Eds.), Superalloys 2020, Springer International Publishing, 2020, pp. 408–420.

[66] S. Murray, K. Pusch, A. Polonsky, C. Torbet, G. Sweard, N. Zhou, S. Forsik, P. Nandwana, M. Kirka, R. Dehoff, W. Slye, T. Pollock, A defect-resistant CoNi superalloy for 3D printing, Nature Commun. 11 (2020) 4975.

[67] J. Xu, H. Brodin, R.L. Peng, V. Luzin, J. Moverare, Effect of heat treatment temperature on the microstructural evolution of CM247LC superalloy by laser powder bed fusion, Mater. Charact. 185 (2022) 111742.

[68] L.M. Suave, J. Cormier, P. Villechaise, A. Soula, Z. Hervier, D. Bertheau, J. Laigo, Microstructural evolutions during thermal aging of alloy 625: Impact of temperature and forming process, Metall. Mater. Trans. A 45 (2014) 2963–2982.

[69] H. Gruber, M. Henriksson, E. Hryha, L. Nyborg, Effect of powder recycling in electron beam melting on the surface chemistry of alloy 718 powder, Metall. Mater. Trans. A 50 (2019) 4410–4422.

[70] G. Soundarapandiyan, C. Johnston, R.H. Khan, C.L.A. Leung, P.D. Lee, E. Hernandez-Nava, B. Chen, M.E. Fitzpatrick, The effects of powder reuse on the mechanical response of electron beam additively manufactured Ti6Al4V parts, Addit. Manuf. 46 (2021) 102101.

[71] H. Li, J. Sun, M. Hardy, H. Evans, S. Williams, T. Doel, P. Bowen, Effects of microstructure on high temperature dwell fatigue crack growth in a coarse grain P/M nickel based superalloy, Acta Mater. 90 (2015) 355–369.

[72] N. Zhou, A.D. Dicus, S.A.J. Forsik, T. Wang, G.A. Colombo, M.E. Epler, Development of a new alumina-forming crack-resistant high-γ' fraction Ni-base superalloy for additive manufacturing, in: S. Tin, M. Hardy, J. Clews, J. Cormier, Q. Feng, J. Marcin, C. O'Brien, A. Suzuki (Eds.), Superalloys 2020, Springer International Publishing, Cham, 2020, pp. 1046–1054.

[73] J. Xu, Alloy Design and Characterization of γ ' Strengthened Nickel-based Superalloys for Additive Manufacturing (Ph.D. thesis), Linköping University, 2021.

[74] J.N. Ghoussoub, P. Klups, W.J. Dick-Cleland, K.E. Rankin, S. Utada, P.A. Bagot, D.G. McCartney, Y.T. Tang, R. C.Reed, A new class of alumina-forming superalloy for 3D printing, Addit. Manuf. 52 (2022) 102608.

[75] S.P. Murray, E.B. Raeker, K.M. Pusch, C. Frey, C.J. Torbet, N. Zhou, S.A.J. Forsik, A.D. Dicus, G.A. Colombo, M.M. Kirka, T.M. Pollock, Microstructure evolution and tensile properties of a selectively laser melted CoNi-base superalloy, Metall. Mater. Trans. A 53 (2022) 2943–3960.